SNR Efficiency of Combined Bipolar Gradient Echoes: Comparison of 3D FLASH, MPRAGE, and Multi-Parameter Mapping with VFA-FLASH and MP2RAGE

Jean-David Jutras[1], Keith Wachowicz[1,2], Guillaume Gilbert[3], Nicola De Zanche[1,2,*]

1. Department of Oncology, University of Alberta, Edmonton, Alberta, Canada
2. Department of Medical Physics, Cross Cancer Institute, Edmonton, Alberta, Canada
3. MR Clinical Science, Philips Healthcare Canada, Markham, Ontario, Canada

Published in

Magnetic Resonance in Medicine

DOI: 10.1002/mrm.26306

***Corresponding author:**

Nicola De Zanche
Department of Medical Physics
Cross Cancer Institute
11560 University Avenue
Edmonton, Alberta, Canada
T6G 1Z2

Email: dezanche@ualberta.ca

Abstract

Purpose

High-bandwidth bipolar multi-echo gradient-echo sequences are increasingly popular in structural brain imaging because of reduced water-fat shifts, lower susceptibility effects and improved SNR efficiency. In this work, we investigate the performance of three 3D multi-echo sequences (MPRAGE, MP2RAGE, and FLASH) with scan times <9 min and 1mm-isotropic resolution against their single-echo, low-bandwidth counterparts at 3T. We also compare the performance of multi-parameter mapping (PD, T_1 and T_2^*) with bipolar multi-echo MP2RAGE versus the variable flip angle technique with multi-echo FLASH (VFA-FLASH).

Methods

Multi-echo sequences are optimized to yield equivalent contrast and improved SNR compared to their single-echo counterparts. Theoretical SNR gains are verified with measurements in a multi-layered phantom. Robust image processing pipelines extract PD, T_1 and T_2^* maps from MP2RAGE or VFA-FLASH and corresponding SNR is measured with varying SENSE accelerations ($R=1–5$) and number of echoes ($N=1–12$). All sequences are also tested on four healthy volunteers.

Results

Multi-echo sequences achieve SNR gains of 1.3–1.6 over single-echo. MP2RAGE yields comparable T_1-to-noise ratio to VFA-FLASH, but significantly lower SNR (< 50%) in PD and T_2^* maps. Measured SNR gains agree with the theoretical predictions for SENSE accelerations <3.

Conclusion

Multi-echo sequences achieve higher SNR efficiency over conventional single-echo sequences, despite 3-fold higher sampling bandwidths. VFA-FLASH surpasses MP2RAGE in its ability to map 3 parameters with high SNR and 1mm-isotropic resolution in a clinically relevant scan time (~8:30 min), while MP2RAGE yields lower inter-subject variability in T_1.

Introduction

In recent years, bipolar multi-echo gradient echo pulse sequences have become increasingly popular for 3D structural brain imaging. The main benefits of these sequences include increased SNR and reduced susceptibility-induced geometrical distortions and water-fat shifts (1), both of which become more problematic at high fields. Mitigating these off-resonance effects is of interest in the field of Radiation Therapy Planning (RTP), where geometrical distortions can lead to errors in dose delivery (2), (3). With current gradient performance, and the implementation of regularized parallel imaging (4), it becomes possible to execute pulse sequences such as the Fast-Low-Angle-Shot (FLASH) (5) and the Magnetization-Prepared RApid Gradient Echo (MPRAGE) (6) with high-bandwidth multi-echo trains, while maintaining equal or better SNR efficiency (defined as SNR per square-root of the total scan duration) than the traditional single-echo, low-bandwidth counterparts.

The additional information provided by the multiple echoes can be used to improve the accuracy of image segmentation algorithms (7). For example, Fischl et al (7) have found that a multi-echo FLASH sequence out-performs a conventional single-echo MPRAGE when applied to sub-cortical brain segmentation. Van Der Kouwe et al optimized a multi-echo MPRAGE sequence and compared it to a conventional single-echo MPRAGE in a segmentation study (8), concluding that multi-echo provides considerable benefits, (such as reduced brain volume changes across different scanners) with few drawbacks.

Another common application of bipolar multi-echo sequences is multi-parameter mapping (MPM, i.e., mapping the proton-density PD, T_1 and T_2^* relaxation) using the variable flip angle (VFA) technique (9), (10), (11). Weiskopf et al. have made use of such sequences to map PD^*, T_1, T_2^* and magnetization transfer (MT) within a reasonable scan time <18 min at 3T (12). These quantitative parameters can then be re-combined to create synthetic images containing FLASH, MPRAGE or other arbitrary types of contrast (13), (14).

The recent "MP2RAGE" variant of the traditional MPRAGE has been proposed for structural brain imaging (15). Its two acquisition blocks follow a shared inversion-recovery module, leading to a T_1-weighted image, and a PD-weighted image. The two complex image signals are combined analytically to obtain a real image that is both purely T_1-weighted and bias-field corrected (fully corrected for the receive B_1 and to a first order for the transmit B_1). A T_1 map can be calculated via a look-up table and if multiple echoes are acquired, T_2^* and PD mapping are also possible. An MPM pipeline with MP2RAGE was also recently proposed to map T_1, T_2^* and quantitative susceptibility mapping (QSM) using unipolar echoes (16).

To our knowledge, comparisons of the SNR efficiency of MP2RAGE versus the VFA technique, or of conventional single-echo vs. bipolar multi-echo MPRAGE or FLASH sequences have yet to be reported. Furthermore, the literature lacks a consensus on how multiple bipolar echoes should be combined to maximize SNR or CNR (i.e., averaging the echoes (1), a root-sum-of-squares combination (8), or a weighted linear combination (8)). Therefore, we begin our analysis by showing that the root-sum-of-squares (RSS) is optimal for combining magnitude images at different echo times (multi-echo recombined gradient echo, known in the industry as MERGE, MEDIC or mFFE), and calculate the consequent SNR gains. We then optimize and test 3D MPRAGE, MP2RAGE and FLASH sequences with high bandwidths and multiple bipolar echoes to yield superior SNR efficiency than their single-echo, low-bandwidth counterparts (each with identical scan times under 9 min). We also propose and test two MPM pipelines: one based on a multi-echo (bipolar) MP2RAGE and the second based on the VFA technique with multi-echo (bipolar) FLASH (abbreviated "VFA-FLASH"). For FLASH and MPRAGE, the measured SNR gains are compared to the theoretical predictions, while for the quantitative MPM pipelines (with MP2RAGE and VFA-FLASH) their SNR efficiency (in PD, T_1 and T_2^* maps) is compared. Both MPM pipelines are also tested in vivo on four volunteers.

THEORY

SNR OF SINGLE-ECHO SPOILED GRADIENT-ECHO

The SNR in standard expressions is proportional to the square-root of the total acquisition time, or inversely proportional to the square-root of the readout bandwidth (17), assuming T_2^* decay is negligible within the acquisition window, T_{acq}. Without this assumption, different expressions have been reported in the literature. Vinitski et al (18) derived an expression relating SNR of a spin-echo sequence to T_2, T_2^*, T_{acq} and TE, which may be modified for a spoiled gradient-echo pulse sequence by replacing T_2 with T_2^* in the TE exponential term to yield,

$$SNR \propto \frac{2T_2^*(1-e^{-T_{acq}/2T_2^*})e^{-TE/T_2^*}}{\sqrt{T_{acq}}}, \tag{1}$$

where TE is the echo time. When T_2^*>>T_{acq}, we can approximate the exponential terms as $\exp(-T_{acq}/2T_2^*) \approx 1 - T_{acq}/2T_2^*$, and $\exp(-TE/T_2^*) \approx 1$, such that $SNR \propto \sqrt{T_{acq}}$ as expected. Fleysher et al (19) state that $SNR \propto \sqrt{T_{acq}} \exp(-T_{acq}/2T_2^*)$, which may be reconciled with Eq. (1) by making the first assumption above as well as $TE \approx T_{acq}/2$. Finally, Rahmer et al (20) state that $SNR \propto P_{tot}(0)\sqrt{T_{acq}}$, where $P_{tot}(0)$ is the total point-spread-function (PSF) evaluated at the center of a voxel, and the SNR for full-echo Cartesian sampling becomes $SNR \propto (1-e^{-T_{acq}/T_2^*})/\sqrt{T_{acq}/T_2^*}$ for a point-like object. The optimal acquisition window for these three expressions ranges between $T_{acq}=0.6795\ T_2^*$ (Vinitski), $T_{acq}=T_2^*$ (Fleysher) and $T_{acq}=1.2564\ T_2^*$ (Rahmer). In this work we use Fleysher's expression since it is simpler and better matches phantom measurements (see the supporting online material).

SNR OF MULTI-ECHO SPOILED GRADIENT-ECHO

When images resulting from multiple echoes of the same bandwidth are acquired within a FLASH (a.k.a. SPGR, T_1FFE, GRE) sequence, Eq. (1) applies to each echo (if SNR is high enough so that the noise assumes a Gaussian distribution (21)). As shown in Appendix A, assuming a mono-exponential T_2^* decay the SNR gain (relative to the first echo) obtained through the RSS combination is

$$G_{SNR} = \frac{\sqrt{\sum_{n=1}^{N} e^{-2TE_n/T_2^*}}}{e^{-TE_1/T_2^*}}, \tag{2}$$

where N is the total number of sampled echoes. In Appendix A it is also shown that the RSS combination provides the highest possible SNR gain, outperforming averaging (1). This is not the case for multi-echo MP2RAGE (Appendix B) where, instead, a real MP2RAGE image must be calculated first for each echo, and all are then combined using a weighted average ($MP2RAGE_{wav}$).

Multiplying Eq. (1) by the SNR gain of Eq. (2) yields the SNR in the MERGE combination image,

$$
\begin{aligned}
&SNR_{ME} \propto \frac{2\,T_2^*}{\sqrt{T_{acq}}}(1-e^{-T_{acq}/2T_2^*})\sqrt{\sum_{n=1}^{N} e^{-2TE_n/T_2^*}} \quad \text{(Vinitski)} \\
&SNR_{ME} \propto \sqrt{T_{acq}}\sqrt{\sum_{n=1}^{N} e^{-2TE_n/T_2^*}} \quad \text{(Fleysher)}
\end{aligned} \quad . \tag{3}
$$

Deriving an expression for the SNR as a function of the acquisition time requires knowledge of the limitations of scanner hardware, such as the amount of dead-time, Δ, required for the RF pulse excitation, the durations of the phase-encoding step and gradient ramp prior to the first echo, as well as the time, τ, required for the gradients to ramp up and down between successive acquisition windows. Our Philips 3T Achieva scanner uses a maximum gradient strength of ~21 mT/m and a slew rate of ~100 T/(s m). The minimum echo time can be written as $TE_{min}=\Delta+T_{acq}/2$, where $\Delta\approx1.3$ ms using a 2-lobe sinc RF excitation pulse. The n^{th} echo time can be expressed as $TE_n=TE_{min}+(n-1)(T_{acq}+\tau)$, where $\tau\approx0.4$ ms is also essentially independent of T_{acq}. Setting $TR >> T_2^*$ (e.g., $TR > 200$ ms) allows the acquisition of a large number of echoes and nearly full T_2^* decay before the following excitation pulse. As $N\to\infty$ Eq. (3) rapidly converges to (see Appendix C)

$$
\begin{aligned}
&SNR_{ME} \propto \frac{2T_2^*}{\sqrt{T_{acq}}}(1-e^{-T_{acq}/2T_2^*})\sqrt{\frac{e^{-2\Delta/T_2^*}e^{-T_{acq}/T_2^*}}{1-e^{-2(T_{acq}+\tau)/T_2^*}}} \quad \text{(Vinitski)} \\
&SNR_{ME} \propto \sqrt{T_{acq}}\sqrt{\frac{e^{-2\Delta/T_2^*}e^{-T_{acq}/T_2^*}}{1-e^{-2(T_{acq}+\tau)/T_2^*}}} \quad \text{(Fleysher)}
\end{aligned} \quad . \tag{4}
$$

At sufficiently long acquisition times the SNRs of MERGE (Eq. (4)) and single-echo FLASH (Eq. (1)) with the same TR and flip angle converge as shown in Figure 1(a) for various values of T_2^*. In MERGE, (assuming a sufficient number of echoes for the SNR to converge), the SNR reaches a maximum theoretical value (calculated from the first derivative of Eq. (4)), at an optimal T_{acq} which also depends on the T_2^*, but, as illustrated in Figure 1(a), is significantly shorter than that of a single echo, especially for longer T_2^* values. This permits significant SNR gains while using short acquisition windows to minimize image distortions induced by B_0 inhomogeneity and other off-resonance effects.

<Fig. 1>

Comparison to Signal Averaging and TR increases in FLASH

The signal in an ideally-spoiled gradient echo (SPGR) or FLASH is given by (22), p. 587

$$S(TR, TE, \alpha) \propto PD \frac{(1-E_1)\sin\alpha}{1-E_1\cos\alpha} e^{-TE/T_2^*}, \tag{5}$$

where α is the flip angle, $E_1 = \exp(-TR/T_1)$, and PD is the proton density. This proportionality also holds for the n^{th} echo in MERGE by substituting TE with TE_n, and the combined MERGE signal is given by multiplying Eq. (5) by Eq. (2).

Signal averaging yields an SNR gain of $\sqrt{NEX}$ (since noise in different datasets is uncorrelated), while total scan time increases in proportion to the number of experiments or averages (NEX). Another way to increase the SNR in Eq. (5) is to increase the TR and readjust the flip angle so that it remains equal to the Ernst angle (or the same ratio relative to the maximum signal), for a given T_1 of interest. This yields an SNR gain $\approx \sqrt{TR_2/TR_1}$, where $TR_2 > TR_1$ assuming $TR << T_1$ (see (22), p. 691), and consequently does not confer any SNR advantage over averaging for the same total scan time. However, increasing the TR creates room for sampling more echoes, which provides an additional SNR boost through Eq. (2).

Using Fleysher's simplification of Eq. (1), and accounting for the parallel imaging acceleration factor R and geometry factor g, the expected SNR in a FLASH sequence is

$$SNR_{\text{FLASH}} \propto \frac{\sqrt{T_{acq}}}{g\sqrt{R}} \cdot \frac{(1-E_1)\sin\alpha}{1-E_1\cos\alpha} D(TE;T_2^*), \quad D = \begin{cases} e^{-TE/T_2^*}, & \text{single echo} \\ \sqrt{\sum_{n=1}^{N} e^{-2TE_n/T_2^*}}, & \text{N echoes in RSS} \end{cases}. \tag{6}$$

In Figure 1(b), Eq. (6) was used to plot the SNR efficiency vs TR for a multi-echo bipolar FLASH compared to a typical single-echo FLASH (assuming R=1, g=1). While a single-echo FLASH with T_{acq}>6 ms would suffer from unacceptable geometrical distortions, the multi-echo FLASH (with MERGE/RSS combination) conserves SNR at short T_2^*, and predicts a ~1.6-fold SNR gain in GM/WM tissues (T_1/T_2^*=1200/50 ms), at TR~30 ms. Similar analytical expressions can be written for the SNR in MPRAGE and MP2RAGE using the signal equation (S_{MPRAGE}) derived by Deichmann (23) and the two MP2RAGE signals (GRE_{TI1} and GRE_{TI2}) derived by Marques (15):

$$SNR_{\mathrm{MPRAGE}} \propto \frac{\sqrt{T_{acq}}}{g\sqrt{R}} S_{\mathrm{MPRAGE}}(\alpha, TR, TI, TD, TR_{MP}) D(TE; T_2^*), \tag{7}$$

$$SNR_{\mathrm{MP2RAGE}} \propto \frac{\sqrt{T_{acq}}}{g\sqrt{R}} \cdot \frac{\Re\,[GRE_{TI_1}^{*} GRE_{TI_2}]}{\left|GRE_{TI_1}\right|^2 + \left|GRE_{TI_2}\right|^2} D(TE; T_2^*) \Bigg/ \sqrt{\frac{\left(\left|GRE_{TI_1}\right|^2 - \left|GRE_{TI_2}\right|^2\right)^2}{\left(\left|GRE_{TI_1}\right|^2 + \left|GRE_{TI_2}\right|^2\right)^3}}\,. \tag{8}$$

Here, $GRE_{TI} = GRE_{TI}(\alpha, TR, TFE, TA, TB, TC, TR_{MP})$, where TI is the inversion time, TR_{MP} is the shot duration, TD is the recovery (a.k.a. delay) time, and TFE is the turbo field echo factor (i.e., number of excitations per acquisition block, denoted n by Marques). TA, TB and TC are, respectively, delay times before, between and after the two acquisition blocks in MP2RAGE as defined in Ref. (15). For a derivation of Eq. (8), see Appendix B and recall that in this case the optimal combination of echoes is not the RSS.

Note that the combined real MP2RAGE image is constrained within the bounds [-0.5, 0.5] (see Ref. (15) and Appendix B). Because of this scaling, SNR measurements on this image are not readily comparable to those of standard images. To compare the SNR efficiency of MP2RAGE with VFA-FLASH, it is therefore appropriate to first convert the normalized image to a T_1 map, and then compare the T_1-to-noise ratio (T_1NR), of each technique (defined as T_1 divided by its standard deviation σ_{T1}). If the look-up table is sufficiently sampled, we can assume $\sigma_{\mathrm{MP2RAGE}} \propto \sigma_{\mathrm{T1}}$, and calculate a theoretical SNR gain (between two different MP2RAGE protocols) from the ratio of their $\sigma_{MP2RAGE}$. The theoretical SNR gain can then be compared to the SNR gain measured from the T_1 maps by using Eqs. (B3) and (B6).

Multi-Parameter Mapping with VFA-FLASH

In the VFA technique, a linearized version of Eq. (5) is used to solve for T_1 and PD using two optimized flip angles while keeping all other scan parameters identical (9),(24),(25),(26),(27). The two flip angles α_1 and α_2 may be chosen to maximize the accuracy and T_1NR for a T_1 value of interest from a simple analytical expression (see Eq. 11 in Ref. (28), or (29)). Alternatively, the flip angles can be chosen to maximize the SNR of the proton-density map PD (30).

To curve-fit the FLASH datasets, a procedure similar to that of Yarnykh (31) and Deoni (28) for single-echo FLASH images is used to obtain the linearized equation

$$\frac{S_{ME}}{\sin(c_{RF}^{+}\alpha_{nom})} = E_1 \frac{S_{ME}}{\tan(c_{RF}^{+}\alpha_{nom})} + c_{RF}^{-}\, PD(1-E_1)\sqrt{\sum_{n=1}^{N} e^{-2TE_n/T_2^*}}, \qquad S_{ME} = \sqrt{\sum_{n=1}^{N} S_n^2}, \tag{9}$$

where c_{RF}^{+} is a correction factor for flip-angle inhomogeneity (B_1^{+}) given by the ratio of the actual to the nominal flip angle (i.e., α/α_{nom}) (31), c_{RF}^{-} is the correction factor for the receive sensitivity profile (B_1^{-}), and S_{ME} is the MERGE image. Equation (9) is a linear equation ($y=m\,x+b$) with slope E_1 and intercept given by the last term, from which T_1 and PD, respectively, are obtained. Note how the MERGE combination changes the y-intercept, replacing the usual exp($-TE/T_2^*$) decay term with the new SNR gain of Eq. (2). Appendix D shows that this SNR gain will propagate into the final T_1 and PD maps, thus making the best use of available information to maximize the final T_1NR and PDNR (defined similarly to T_1NR above). Curve fitting the N echoes by ordinary least squares yields T_2^*, as implemented in the MPM pipeline of Weiskopf et al (12).

At lower field strengths (≤1.5 T), the B_1 inhomogeneity is often ignored and it is assumed that $c_{RF}^{+} \approx c_{RF}^{-} = c_{RF}$, provided that an optimal-SNR channel combination with uniform sensitivity is performed (32). If T_1 and PD are calculated without correcting for the flip-angle non-uniformities and receiver bias, *apparent* T_1 and PD will result (30)

$$T_1^{app} \approx \left(c_{RF}^{+}\right)^2 T_1, \quad PD^{app} \approx c_{RF}^{+} c_{RF}^{-} PD. \tag{10 a, b}$$

Two bias fields denoted by

$$\Psi_{\mathrm{T1}} \propto (c_{RF}^{+})^2, \quad \Psi_{\mathrm{PD}} \propto c_{RF}^{+} c_{RF}^{-}, \tag{11a, b}$$

can be fitted from the T_1^{app} and PD^{app} map, respectively, by employing a bias field correction algorithm, followed by a calibration step (33), (34). A scanner-dependent calibration factor $\langle c_{RF} \rangle$, defined as the mean flip angle, $\langle \alpha_{meas} \rangle$, measured over the brain (using a skull-stripped binary mask), divided by the nominal flip angle (α_{nom}, set on the console) is also needed to convert the bias field into a B_1 map. (Weiskopf et al found that the assumption $\langle c_{RF} \rangle=1$ holds well for a Siemens TIM Trio (33), while for our scanner we found $<c_{RF}> \approx 0.97$). This approach has the significant advantage of not requiring the acquisition of a separate B_1 map (and the associated increase in total scan time), hence maintaining the best theoretical SNR efficiency. Similarly to (33) (34), our post-processing pipeline includes a bias-field correction algorithm, N4ITK (35), which is more widely applicable because it does not rely on a human brain atlas like SPM8 used in the above references.

Since the T_2^* map tends to be noisy due to the uncertainty in curve-fitting, and the last factor of the intercept must be divided out to obtain PD, the T_2^* map should be filtered or de-noised (with edge-preserving techniques such as a median filter (36), p. 10, or gradient anisotropic diffusion de-noising (37)) prior to solving for PD. Moreover, since one T_2^* map is obtained at each flip angle, the weighted average T_2^* may be calculated to improve its SNR using weights proportional to the inverse of the noise variance (see Appendix E)

$$T^*_{2,final} = \frac{w_1 T_2^*(\alpha_1) + w_2 T_2^*(\alpha_2)}{w_1 + w_2}, \qquad w_i = \frac{\sin^2(\alpha_i)}{(1 - E_1 \cos(\alpha_i))^2}. \tag{12}$$

If motion is not negligible, an advanced combination procedure for the T_2^* maps has been recently proposed to minimize the resulting artifacts (38). A summary of the post-processing steps involved in the calculation of T_1, PD and T_2^* is given in Figure 2(a).

Multi-Parameter Mapping with MP2RAGE

A multi-echo MP2RAGE provides two T_2^* maps: one via least-squares fitting of the $|GRE_{TI1}(TE_n)|$ images, and the second using the $|GRE_{TI2}(TE_n)|$ images. However, the presence of a null point in the $|GRE_{TI1}(TE_n)|$ images leads to very poor T_2^*NR, and in practice only the other set results in a useable T_2^* map.

The T_1 map is calculated via a 1D look-up table of the real MP2RAGE signal (15), because an explicit expression for T_1 as a function of signal and scan parameters does not exist. However, the table is not bijective for very long T_1 (the MP2RAGE signal as a function of T_1 attains a minimum at $T_{1max} \approx 2700$), and consequently the T_1 of CSF will be aliased to lower values (e.g. 2500 ms instead of the correct 4500 ms).

Once both T_2^* and T_1 are known, two different PD maps may be obtained in theory: one from the $GRE_{TI1}(TE_n)$ images (PD_1), and the second from the $GRE_{TI2}(TE_n)$ images (PD_2). It makes sense to first combine the multiple echoes at TI_1 or TI_2 in RSS, to yield MERGE combinations ME_{TI1} and ME_{TI2} with higher SNR. Two issues must be resolved: the PDNR in PD_1 will be very poor close to the signal null, and secondly, T_1 aliasing in CSF will bias the measured PD. Performing a weighted sum of PD_1 or PD_2 is not advantageous (see Supporting Online Information), while choosing only PD_1 or PD_2 leads to a bias in the PD of CSF, because (relative to PD^{water} =100%) T_1 aliasing in long T_1 results in PD_1^{CSF}>100%, and PD_2^{CSF}<100%. Therefore we choose a threshold $T_1^{ref} < T_{1max}$, and set $PD=PD_2$ if $T_1 \leq T_1^{ref}$ and $PD=PD_1$ if $T_1>T_1^{ref}$, accepting that in CSF an overestimated PD is preferable over an underestimated PD, because it prevents CSF from being confounded with surrounding tissues.

In summary, using the equations derived by Marques et al (15), the final expression for the proton density is then:

$$PD = \begin{cases} \dfrac{ME_{\mathrm{TI1}}}{c_{RF}^{-}\,\sin(c_{RF}^{+}\alpha_1)\sqrt{\sum_{n=1}^{N} e^{-2TE_n/T_2^*}}} \left[\dfrac{-\varepsilon_{inv}\, m_{ss}\, EA + (1-EA)}{(\cos(c_{RF}^{+}\alpha_1)E_1)^{1-TFE/2}} + (1-E_1)\dfrac{1-(\cos(c_{RF}^{+}\alpha_1)E_1)^{TFE/2-1}}{1-\cos(c_{RF}^{+}\alpha_1)E_1} \right]^{-1}, & T_1 > T_1^{ref} \\ \dfrac{ME_{\mathrm{TI2}}}{c_{RF}^{-}\,\sin(c_{RF}^{+}\alpha_2)\sqrt{\sum_{n=1}^{N} e^{-2TE_n/T_2^*}}} \left[\dfrac{m_{ss} - (1-EC)}{EC\,(\cos(c_{RF}^{+}\alpha_2)E_1)^{TFE/2}} - (1-E_1)\dfrac{(\cos(c_{RF}^{+}\alpha_2)E_1)^{-TFE/2} - 1}{1-\cos(c_{RF}^{+}\alpha_2)E_1} \right]^{-1}, & T_1 \leq T_1^{ref} \end{cases}$$

, (13)

where $m_{ss}=m_{z,ss}/PD$ is the normalized steady-state longitudinal magnetization derived in Ref. (15), ε_{inv} is the inversion efficiency, $EA=exp(-TA/T_1)$ and $EC=exp(-TC/T_1)$. We chose T_1^{ref}=2000 ms, and employed N4ITK to estimate the bias field on the PD^{app} image and remove the c_{RF}^+ and c_{RF}^- inhomogeneity. As in the case of the MPM pipeline with VFA-FLASH, the T_2^* map must be filtered to prevent adding noise to the PD map. The post-processing steps for MPM with MP2RAGE are shown in Figure 2(b).

<Fig. 2>

METHODS

To verify the theory developed in Eqs. (1)–(4), SNR measurements were performed in phantoms with methods and results given in the online supporting information (see Supporting Figure S2).

Optimization of MPRAGE, FLASH, MP2RAGE and VFA-FLASH

All 3D MRI protocols were optimized based on a total scan time constraint of ~8:30 min, except for the single-echo and 8-echo FLASH sequences, as shown in Table 1. In all cases, the field-of-view (FOV) was 240×240×170 mm^3, with 1 mm isotropic resolution and non-selective RF pulses. The bandwidth of the single-echo protocols was chosen (175 or 180 Hz/pix depending on system timing constraints) based on the maximum geometrical distortion and water-fat shifts considered tolerable for RTP at 3T (39). (Howarth et al recommend a bandwidth ≥100 Hz/pix in structural brain imaging at 1.5T (40)). Except for the single-echo MP2RAGE, all echo times were selected to have water in-phase with fat ($TE = n \times 2.3$ ms), and for the multi-echo bipolar sequences, the bandwidths (517 or 540 Hz/pix, respectively) were adjusted to maximize the sampling efficiency (ε, defined as total sampling time divided by total scan time) within the limits of the system's gradient performance.

Both the single-echo and the 6-echo MPRAGE (denoted as MPR1 and MPR6) were optimized to yield a similar contrast and signal evolution (for best gray- and white-matter CNR) by performing simulations based on the recursive solution of the Bloch equations as done in Ref. (41). For MP2RAGE, the protocol optimized by Marques et al (protocol #1 in Table 1 of Ref. (15)) was taken as a starting point. Using similar Bloch equation simulations TR_{MP}, TFE, TI_1 and TI_2 were re-optimized so that the resulting multi-echo protocol (MP2R6) would suffer minimal off-resonance effects, have high SNR efficiency and enable T_2^* and PD mapping, without exceeding the maximum amount of SENSE acceleration (2.5 × 2 = 5-fold) possible with the 8-channel head array. A phantom T_1NR comparison of the MP2R1 protocol (listed in Table 1) with the 5 protocols of Marques et al (15) is provided in online Supporting Figure S3.

For VFA-FLASH, four different protocols were tested with varying number of echoes N, and SENSE acceleration factors (~1.44-fold, 2-fold, 3-fold and 4-fold) to assess their effects on the quality (and SNR) of the quantitative maps. The nominal flip angles were selected to maximize the T_1NR at a reference T_1 of ~1200 ms (between GM and WM at 3T), using an analytical expression (Eq. 11 in Ref. (28), or (29)), while for the conventional FLASH protocols (FLASH1 and FLASH8), the higher flip angle (α_2) multiplied by a factor of ~1.2 was used to yield good T_1-weighting and SNR. An elliptical phase-encoding k-space shutter was employed in all FLASH sequences to help reduce the total scan time.

<Table 1>

SNR, T_1, PD AND T_2^* MEASUREMENTS IN A MULTILAYERED AGAR PHANTOM

A phantom consisting of 5 differentially-doped agar layers (designed to mimic fat, WM, GM, GM-CSF and CSF) was built to make T_1, T_2^* and SNR measurements with the 10 protocols given in Table 1. Phantom composition was inspired by Ref. (42) (Fixed agar/NaN_3 concentrations of 10/0.5 g/L and varying $MnCl_2$ concentrations of 200, 64, 32, 10 and 0 µM, separated by cellophane wrap to avoid diffusion across the 5 layers). The T_1 of each layer was measured using a gold-standard 2D IR-EPI sequence (FOV=120×172 mm^2, axial slice, resolution: 1.3×1.3 mm^2, slice thickness: 5 mm, TR/TE=15000/17 ms, EPI factor=9, TI=25, 250, 500, 800, 1200, 1700, 2400 and 3200 ms) curve-fitted to solve for T_1 according to Eq. 1 in Ref. (43). The T_2^* was measured in a central slice using the 2D SPGR pulse sequence (32 echoes at the shortest T_{acq}) described in the previous section.

A B_1 map was obtained using Actual Flip Angle Imaging (AFI) (31) with the following parameters: FOV=240×240×170 mm^3, 3.5×5×5 mm^3 voxels, $TR_1/TR_2/TE$ = 25/125/2.8 ms, α=60°, RF phase cycle increment ϕ=150°, BW=220 Hz/pixel, scan time=3 min. The AFI source images were first zero-padded to 128×128×68, c_{RF}^+ was calculated and smoothed using the *smooth3* function in MATLAB (5×5×5 3D Gaussian filter), and finally resampled to 256×256×180 pixels. The calibration constant $<c_{RF}>$ needed to correctly scale Ψ_{T1} into a c_{RF}^+ map was obtained by measuring the mean flip angle $<\alpha_{meas}>$ over the AFI B_1 map (excluding the air cavities) relative to the nominal value α_{nom} (i.e., $<c_{RF}>=<\alpha_{meas}>/\alpha_{nom}$) and found to be $<c_{RF}>$=0.84. N4ITK was unable to remove the inhomogeneity in the T_1^{app} map (since the "staircase" contrast features of the phantom are not sufficiently sparse and are confounded with the B_1 field), therefore in this case the PD^{app} was used to estimate Ψ_{T1} instead, and RF symmetry assumed (i.e., $c_{RF}^+ \approx c_{RF}^- = c_{RF}$, and $\Psi_{T1}=\Psi_{PD}$, which holds well because of the low conductivity of agar (44)).

The T_1 measured with VFA-FLASH (VFA-FLASH1, 6, 9 and 12) were compared to MP2RAGE (MP2R1 and 6) and 2D IR-EPI (Supporting Figure S5). The SNR of each layer was measured as the ratio of mean signal S (or the mean T_1, PD, T_2^*, as applicable), and noise standard deviation σ (or σ_{T1}, σ_{PD}, σ_{T2*}), in five 3D ROIs of 31×31×5 pixels (taken, respectively, at the center and at the four corners of the phantom as shown in Supporting Figure S4) of each agar layer using the

ROI-FFT method. The standard deviation of the five SNR measurements was used as error estimate in each layer. The SNR gains from FLASH8 over FLASH1 and from MPR6 over MPR1 were measured and compared to the predicted values using Eqs. (6), (7), and (8), assuming an idealized average geometry factor of g=1 using regularized SENSE (4). Prior to measuring SNR, the MPRAGE images were bias-corrected approximately by dividing them by c_{RF}^2. The SNR in the parametric maps (T_1NR, T_2^*NR and PDNR) were also compared across the various MPM protocols, and T_1NR gains were compared to the theoretical predictions for MP2R6 over MP2R1 and for VFA-FLASH6, 9 and 12 over VFA-FLASH1 (using the equations in Appendix B and Appendix D).

IN VIVO BRAIN IMAGING ON 4 VOLUNTEERS

The effectiveness of MPM was assessed in vivo on four healthy male volunteers (ages: 26, 31, 41 and 43) after institutional ethics approval and informed consent were obtained. The two MP2RAGE and four VFA-FLASH protocols (total scan time of ~55 min) were tested on volunteer v1. For the remaining volunteers only MP2R1, MP2R6 and VFA-FLASH9 were tested (~29 min scan time). Slight geometrical mismatches can occur when combining even and odd echoes due to the opposite polarity of B_0-induced geometrical distortions. Helms et al recommend using a sampling bandwidth greater than 350 Hz/pixel to minimize such mismatches (1). As a precaution, the even and odd echoes were combined separately to form "even" and "odd" MERGE (or $MP2RAGE_{wav}$ – see Appendix B and Figure 2) images which were then co-registered using deformable B-spline image registration in 3D Slicer (www.slicer.org) (45) prior to combining them to obtain a final MERGE (or $MP2RAGE_{wav}$) image. To compensate for possible slight head motion between the successive MERGE datasets at the two nominal flip angles, a rigid registration was also performed to ensure best possible geometrical match between the two final MERGE and T_2^* images. The windowed sinc interpolation kernel was used in every case to avoid loss of resolution or blurring in the final registered images.

Quantitative T_1, T_2^* and PD maps were calculated based on the post-processing workflow summarized in Figure 2. The optimal spline distance and number of iterations of the N4ITK algorithm were determined previously (by minimizing the standard deviations $std(T_1)$ and $std(PD)$ over the corrected WM/GM reference tissues, similarly to Ref. (46)), using data from 8 additional volunteers (4 males and 4 females) scanned with a protocol similar to VFA-FLASH9.

To improve the accuracy of the bias field calculation, only soft tissues, (i.e., excluding air cavities and CSF from the Ψ_{T1} calculation, and also adipose from the Ψ_{PD} calculation) were included, as done in Ref. (46) with the older N3 algorithm. The mask was derived from a fuzzy c-means segmentation (47) of the T_1^{app} image in MATLAB and exported into 3D Slicer. Optimal spline distances were found to be 185 mm for Ψ_{PD}, and 210 mm for Ψ_{T1} with 400, 320, and 240 iterations (eight times the default number: 50, 40, 30). All other parameter settings were left to their default values.

The *PD* map is usually normalized with respect to CSF. However, simulation-based correction factors for non-ideal RF spoiling in CSF are then required (34), (48); moreover, the T_2^* of CSF (needed to solve for *PD*) is usually too long to be accurately measured using a few echoes, and as mentioned previously, MP2RAGE cannot yield accurate *PD* or T_1 measurements in CSF. Therefore, we opted instead to normalize the *PD* map with respect to the mid-point between the average WM and GM peaks of the *PD* histogram (71±1% and 81±1%, respectively measured by various authors and techniques (30), (34), (49). After multiplication by 0.76, the mid-points align correctly at <*PD*>=76%. Finally, *PD*, T_1 and T_2^* histograms (normalized to the total number of head voxels, excluding air cavities) were calculated for each volunteer (excluding the slices below the cerebellum) to provide an overall assessment of the image quality. Measurements of mean *PD*, T_1 and T_2^* were made in manually-contoured ROIs in various brain regions for comparison with previously reported literature values.

RESULTS

SNR, T_1, *PD* AND T_2^* MEASUREMENTS IN THE PHANTOM

Results for the SNR measurements on conventional T_1-weighted images (MPR1, MPR6, FLASH1 and FLASH8) are given as bar graphs in Figure 3(a), along with the SNR gains of the multi-echo protocols over their single-echo counterparts in (b).The measured SNR gains agree with the theory, except in the bottom layer (short T_1/T_2^* mimicking fat) of the FLASH8 image, probably owing to a higher B_1 non-uniformity than in other layers. SNR gains of 1.28 and 1.52 for MPR6 and FLASH8, over MPR1 and FLASH1, respectively, are achieved in layer 3 (T_1/T_2^*=1294/95 ms). Sagittal images of the phantom are shown in Supporting Figure S4. Note how the contrasts in MPR6/ FLASH8 at TE_1 are equivalent to those in MPR1/FLASH1, respectively, despite significantly different scan parameters.

Measured T_1NR of the various MPM protocols are shown in Figure 3(c). It is noteworthy that (except in the bottom and top layers) MP2R1 achieves comparable T_1NR to VFA-FLASH1 in the same total scan time, and likewise, MP2R6 has comparable T_1NR to VFA-FLASH6. However, at short or long T_1=449/2658 ms, VFA-FLASH1/6 slightly outperforms MP2RAGE1/6. Scan times are nearly identical so similar conclusions can be drawn for T_1NR efficiency. The measured gains in T_1NR (multi-echo over single-echo protocols) are compared to the predicted values in Figure 3(d). The measured gains (in layers with T_1=951 and 1294 ms which mimic WM/GM) for the VFA-FLASH12 and MP2R6 protocols are both more modest (~1.69 and 1.33) than predicted (~1.82 and 1.48), but as can be deduced from the error bars, some of the ROIs agreed more closely with the predicted values. The deviation may be due to the large parallel imaging acceleration factors of 4-fold and 4.8-fold in these two protocols, respectively, which strongly violate the assumption $g\approx 1$.

Measured PDNR and T_2^*NR of the different protocols are shown in Figure 3(e) and (f), respectively. Note that *PD* from the single-echo protocols (VFA-FLASH1 and MP2R1) was corrected for T_2^* decay using the T_2^* map derived from the VFA-FLASH9 protocol. As previously predicted in the Theory, the SNR in the *PD* and T_2^* maps derived from MP2RAGE is significantly lower than that from VFA-FLASH. This is well explained by the lower sampling efficiency of MP2RAGE (~36–38%) compared to VFA-FLASH (~70–75%), and the fact that only the second image $|GRE_{TI2}|$ is used to solve for T_2^* and *PD*.

Sagittal *PD*, T_1 and T_2^* maps of the different protocols are shown in Figure 4. The green arrows point to overestimated *PD* at the phantom edges, arising from strong susceptibility effects. The bias field Ψ_{PD} estimated from the PD^{app} in MPR1, as well as the c_{RF} map estimated from PD^{app} in VFA-FLASH are also shown.

Measured T_1 and T_2^* (using the same ROIs), from the various protocols are compared in Supporting Figure S5. There is generally very good agreement across the measurements, and slightly larger differences in the top layer with longest T_1/T_2^*=2658/110 ms. Within that layer, IR-EPI measures a lower T_1 than in all the MPM protocols, likely due to the fact that the approximation $T_1^{app} \approx (c_{RF}^{+})^2\, T_1$ in Eq. (10a) biases the corrected T_1 to longer values at long T_1 and low c_{RF}^{+}.

<Fig. 4>

In Vivo Results

Quantitative Maps

An axial slice of each quantitative (T_1, PD and T_2^*) map derived from 4 different MPM protocols is displayed in Figure 5. The MP2R6 protocol clearly yields lower SNR in PD and T_2^* than VFA-FLASH6. In fact, the T_2^* map is unusable, therefore the T_2^* map from the VFA-FLASH9 protocol was used instead to correct the proton density for T_2^* decay. Good-quality T_2^* mapping from unipolar multi-echo MP2RAGE was recently reported (16), but the total scan time was more than twice as long (~18 min), and the field strength was 7T, which alone provides a significant SNR advantage compared to the present study. The VFA-FLASH12 protocol yields the highest T_2^*NR, but lower-quality PD and T_1 maps. This finding suggests that recovering pure proton-density and T_1 from heavily T_2^*-weighted MERGE datasets is more challenging than with single-echo FLASH images, especially with a large acceleration factor of 2×2. However, if a more advanced curve-fitting procedure (such as a multi-component T_2^* fit) and a high-density receiver coil array (e.g., 32-channel array) were employed, better quantitative maps with higher SNR could be obtained.

The VFA-FLASH9 protocol achieves the best compromise between good T_2^* and PD image quality, and was thus tested on 3 additional volunteers. Sagittal slices of the parametric maps from all four volunteers are shown in Figure 6. The red arrows indicate an overestimation in PD arising from susceptibility effects in the frontal sinuses (resulting in non-exponential T_2^* decay and incorrect G_{SNR} in Eq. (2)). The effect is less pronounced on the VFA-FLASH6 PD maps (not shown in vivo, but visible in Figure 4).

<Fig. 5>

<Fig. 6>

Histograms (PD, T_1 and T_2^*)

Histograms of the parametric maps derived from all MPM protocols tested on volunteer v1 are shown in Figure 7 (a–c), and those from the VFA-FLASH9 protocol tested on four different subjects are displayed in (d–f). The *PD* histograms (Figure 7(b)) of the 9-echo and 12-echo VFA-FLASH protocols are slightly more broadened than those of the 6-echo protocol, which confirms the challenge of recovering pure *PD* from heavily T_2^*-weighted MERGE images. A further explanation is that later echoes are more motion-sensitive than early ones (38). The *PD* histogram from both the VFA-FLASH1 and MP2R1 protocols is also broader, despite excellent WM/GM peak separation. This might be due to the effect of non-ideal RF spoiling previously observed (34), to which a shorter *TR* (=8–11 ms) would be more susceptible because less T_2^* decay can occur between consecutive RF pulses.

The T_1 histogram of MP2R6 also has less GM/WM peak separation than that of MP2R1. Both MP2R1 and MP2R6 were consequently tested on the other three volunteers to confirm this observation (see the *PD* and T_1 histograms of all four volunteers in the online Supporting Figure S6). A plausible explanation is that because MP2RAGE is a phase-sensitive technique, it is more prone to phase errors (inconsistencies between the corresponding echoes at TI_1 vs TI_2), which may be present in such a bipolar multi-echo sequence (50). As shown in Figure 8, both MP2R6 and VFA-FLASH6 show similar trends when separately plotting a T_1 histogram generated from each echo. In both cases, the fat peak shifts significantly depending on the *TE*, with TE_2≈4.6 ms yielding the longest and TE_4/TE_5 ≈9.2/11.4 ms both yielding the shortest adipose T_1. This effect might be explained by the existence of different proton pools within adipose. The T_1 histograms also tend to broaden at longer *TE*, most likely because of reduced SNR. However, the GM peak of the MP2R6 protocol also shows a slight plateau (or second hump) around T_1~1400 ms, which disappears beyond the third echo. Intra- versus extra-cellular water compartments could also be at play, resulting in varying TE-dependent biases in T_1 (51). The effect of B_1^+ inhomogeneity on the T_1 look-up tables of both MP2R1 and MP2R6 is shown in the Supporting Figure S7. Both MP2RAGE protocols were optimized to yield a comparable effect of B_1^+ homogeneity on T_1, and thus the significant differences in histogram shapes must be explained by higher-order effects.

The T_2^* histograms of Figure 7(c) and (f) show that for the MP2R6 protocol the histogram is skewed relative to the VFA protocols because of poor SNR (see bottom-right T_2^* map in Figure 5).

<Fig. 7>

<Fig. 8>

Brain ROI Measurements (PD, T_1 and T_2^*)

Relaxometry measurements in various brain ROIs are listed in Table 2 for the three protocols tested on all four volunteers, along with two reported literature values (representative lower and higher bounds, when available). Except in CSF (i.e., ventricles) *PD* and T_2^* measurements agree well with the literature, and the T_1 measurements also agree with those reported by Marques et al (15) (who use the same MP2RAGE technique).

In general, VFA-FLASH yields ~4% longer T_1 than that from MP2RAGE. The lower T_1 standard deviations measured across the different subjects in MP2RAGE are due to the automatic B_1 bias field correction intrinsic to MP2RAGE, which, unlike VFA-FLASH, is robust to random or subject-dependent fluctuations in RF power calibration in the successive flip angle acquisitions.

The proton density in CSF is overestimated by ~25–27% by MP2R1 and MP2R6, and much less (~10 %) by VFA-FLASH9 (due to a combination of non-ideal RF spoiling (34), and underestimated T_2^* which is clipped at 150 ms instead of the true ~2000 ms). As noted above, in CSF *PD* cannot be measured accurately with MP2RAGE because of the inability to correctly solve for long T_1. The MP2R1 protocol also underestimates *PD* in frontal/occipital WM (~66–67%) compared to the MP2R6 and VFA-FLASH9 (~69–71%).

<Table 2>

DISCUSSION AND CONCLUSIONS

This study compares the SNR efficiency and image quality of bipolar multi-echo gradient echo sequences over their single-echo counterparts (FLASH and MPRAGE). The theory predicts that at 3T, optimized multi-echo sequences can enable SNR and T_1NR gains of 1.3–1.8, despite 3-

fold higher bandwidths, depending especially on the sequence parameters, and on the T_2^*. These gains arise from a combination of increased signal yields (by using longer *TR* and higher flip angles), and the combination of multiple echoes (MERGE). The measured SNR (or T_1NR) gains in the agar phantom agree well with the theory, as long as moderate regularized 2D SENSE accelerations are employed (≤3-fold with an 8-channel head array) which ensures that $g \approx 1$. This hypothesis is confirmed by Lin et al (4) where average g-factors of 0.72, 0.84 and 1.52 were observed for regularized 1D SENSE acceleration with R=2, 2.67, and 4, respectively, using an 8-channel array. Therefore, the lower-than-expected SNR observed in the two protocols with $R \geq 2 \times 2$ (VFA-FLASH12 and MP2R6) is consistent with $g>1$. The 9-echo VFA-FLASH technique was found to achieve the best overall image quality with T_1NR gains of ~1.6, which is comparable to the gain of ~1.67 obtained by a hybrid FLASH-EPI VFA T_1 mapping technique (25).

The SNR efficiency of two MPM pipelines (based on VFA with FLASH, and MP2RAGE) were compared, finding that MP2RAGE yields comparable T_1NR efficiency to that of VFA-FLASH in relevant brain tissues (i.e., WM/GM), despite having only about half the sampling efficiency (35–38% for MP2RAGE, compared to 70–75% for VFA–FLASH). This is readily explained by the fact that the T_1 in MP2RAGE is calculated from a 1D look-up table of the real MP2RAGE signal, which has better T_1-weighting and contrast-to-noise than a standard FLASH image (15). However, since both *PD* and T_2^* must be calculated from magnitude images in either pipeline, VFA-FLASH has a significant SNR advantage (>2-fold) over MP2RAGE for *PD* and T_2^* mapping. Therefore, MP2RAGE is less suitable for MPM applications.

It was recently observed that MP2RAGE also tends to underestimate the WM T_1 (by ~6% at 3T and ~17% at 7T) due to the effect of magnetization transfer, leading to bi-exponential T_1 relaxation (59). In this study, we confirm that MP2RAGE underestimates T_1 by ~4% (3.5%/4.5% for MP2R6/MP2R1) compared to N4ITK-corrected VFA-FLASH (when calculating the average percent difference in the ROI measurements of MP2RAGE vs VFA-FLASH in Table 2). Conversely, in this implementation MP2RAGE yields narrower T_1 variability across different subjects compared to VFA-FLASH (see also Figure 7(d) compared to Supporting Figure S6 (a-b)), most likely because of an intrinsic robustness to random or subject-dependent fluctuations in RF power calibration. Data from Refs. (12), (33), and (60) also suggests that the scan-scan reproducibility of MP2RAGE is better than that of VFA (coefficients of variation (CoV) of 2–3% for MP2RAGE compared to 5–7% for VFA). Further experiments (not shown in this study) revealed that the intra-subject CoV of N4ITK-corrected T_1 from VFA-FLASH is 5.8/7.4% in WM/GM, which compares well with Weiskopf's UNICORT technique (6.5/8.7%) (33), thus ruling out additional random fluctuations due to N4ITK. Improving the scan-scan reproducibility of VFA might be possible by fine-tuning the RF power calibration, or by a subsequent correction based on the expected mean T_1 of WM/GM in the general population (as similarly done for *PD* normalization in this study). The latter approach, however, would suppress differences based on age, gender, and body temperature that have been reported (52), (54), (61). Despite achieving T_1NR gains of ~1.35 over its single-echo counterpart, the 6-echo MP2RAGE results in broader T_1 histogram lines (unless corrected via improved pulse-sequence modeling), thus making it less appealing.

We recommend the use of bipolar multi-echo sequences over their single-echo, low-bandwidth counterparts in structural brain imaging applications where susceptibility-induced geometrical distortions are especially a concern (e.g., Radiation Therapy Planning). Wang et al reported mean and maximum pixel shifts of <0.5mm and <4mm, respectively, at 180 Hz/pixel bandwidth with 3D MPRAGE on 19 patients at 3T (39). The multi-echo MPRAGE or FLASH sequences tested here reduce such geometrical distortions by ~3-fold without SNR penalty and comparable scan times. (Deformable image registration of even and odd echoes was found to be unnecessary in the four volunteers at such high bandwidth, but may be needed in subjects with more substantial susceptibility inhomogeneities such as those due to dental implants).

Despite the more sophisticated post-processing, MPM with VFA-FLASH makes the best use of the increased SNR efficiency and available information to derive parametric maps with high SNR. In closing, we strongly recommend performing SNR validations in a phantom prior to using these bipolar echo sequences routinely because local SNR in images derived from bipolar echo sequences with parallel imaging is heavily dependent on protocol and hardware (especially the g-factors).

Appendix A

Derivation of Equation (2).

The MERGE image is formed by the root-sum-of-squares (RSS) combination of the individual images from each echo similarly to how images from receive arrays are sometimes combined. The SNR of the RSS combination is therefore given by Eq. 9 of (62), where the noise covariance matrix $\mathbf{\Psi}$ is equal to the identity matrix times a constant (σ_0^2) because the MERGE datasets are not acquired simultaneously, but at different times, and noise is therefore uncorrelated.

For a mono-exponential T_2^* decay, the elements of the signal vector are $S_n = S_0 \exp(-TE_n / T_2^*)$, n=1, 2… N and the SNR of the MERGE combination simplifies to

$$SNR_{comb} = \frac{S_0 \sqrt{\sum_{n=1}^{N} \left(e^{-TE_n / T_2^*}\right)^2}}{\sigma_0} = \frac{S_0 \sqrt{\sum_{n=1}^{N} e^{-2TE_n / T_2^*}}}{\sigma_0}. \qquad \text{(A1)}$$

Since the signal at TE=0 (S_0) is not directly measured, we may normalize SNR_{comb} by that of the first echo, SNR_1, such that

$$G_{SNR} = \frac{SNR_{comb}}{SNR_1} = \frac{S_0 \sqrt{\sum_{n=1}^{N} e^{-2TE_n / T_2^*}} \Big/ \sigma_0}{S_0\, e^{-TE_1 / T_2^*} \Big/ \sigma_0} = \frac{\sqrt{\sum_{n=1}^{N} e^{-2TE_n / T_2^*}}}{e^{-TE_1 / T_2^*}}. \qquad \text{(A2)}$$

It is reasonable to think that an optimal linear weighting of the echoes with weights w_i might yield a superior SNR than the simpler RSS combination. In the case of mono-exponential T_2^* decay the optimal weights are equal to the corresponding exponential factors because of the form of $\mathbf{\Psi}$ and because the exponential has the same formal role in the equations as the coil sensitivity does in array image combination (62). We may therefore express the SNR of the combined signal using Eq. 8 or 10 of (62), which simplifies to the same result as above for the RSS combination.

APPENDIX B

As shown by Marques et al (15), letting $x=GRE_{TI1}$, and $y=GRE_{TI2}$ be the two complex MP2RAGE image signals, the optimal signal combination for the real normalized MP2RAGE image is

$$\text{MP2RAGE} = \frac{\Re\left(x^* y\right)}{|x|^2 + |y|^2}, \qquad \text{(B1)}$$

where * denotes complex conjugation, and its noise standard deviation is given by

$$\sigma_{\text{MP2RAGE}} = \sigma_S \sqrt{\frac{\left(x^2 - y^2\right)^2}{\left(x^2 + y^2\right)^3}}, \qquad \text{(B2)}$$

where σ_S is the noise standard deviation in each GRE image (assumed to be equal). Note that $\sigma_S \propto g\sqrt{R} \big/ \sqrt{T_{acq}}$. If multiple echoes are acquired, the T_2^* decay still cancels out in the real normalized MP2RAGE image, but not in its standard deviation. Because the decay function is the same in both images, $x(TE)=X\exp(-TE/T_2^*)$, and $y(TE)=Y\exp(-TE/T_2^*)$, it can be factored out, yielding

$$\sigma_{\text{MP2RAGE}}(TE) = \frac{\sigma_S}{e^{-TE/T_2^*}} \sqrt{\frac{\left(X^2 - Y^2\right)^2}{\left(X^2 + Y^2\right)^3}}. \qquad \text{(B3)}$$

The weighted average is typically calculated by weighing each measurement x_k by the inverse-square of its uncertainty (63) (p. 175)

$$\bar{x} = \frac{\sum_k \frac{x_k}{\sigma_k^2}}{\sum_k 1/\sigma_k^2}. \qquad \text{(B4)}$$

Therefore, the optimal SNR combination of echoes for MP2RAGE is

$$\text{MP2RAGE}_{wav} = \frac{\sum_{n=1}^{N} \text{MP2RAGE}(TE_n) e^{-2TE_n / T_2^*}}{\sum_{n=1}^{N} e^{-2TE_n / T_2^*}}, \tag{B5}$$

and its noise standard deviation is calculated from the uncertainty in a weighted average (63) (p. 176)

$$\sigma_{wav} = \frac{1}{\sqrt{\sum_{n=1}^{N} 1/\sigma^2_{\text{MP2RAGE}}(TE_n)}} = \sqrt{\frac{\left(X^2 - Y^2\right)^2}{\left(X^2 + Y^2\right)^3}} \frac{\sigma_S}{\sqrt{\sum_{n=1}^{N} e^{-2TE_n / T_2^*}}}. \tag{B6}$$

To obtain Eq. (8), we simply divide Eq. (B1) by Eq. (B3) or (B6), for single-echo or a weighted average of multiple echoes, respectively.

APPENDIX C

<u>Derivation of Equation (4).</u>

The square of the SNR gain (Eq. (2)), normalized to the signal at *TE*=0 is

$$\sum_{n=1}^{N} e^{-2TE_n / T_2^*} = \sum_{n=1}^{\infty} e^{-2\left[\Delta - \tau - T_{acq}/2 + n(T_{acq}+\tau)\right]/T_2^*} = e^{-2(\Delta - \tau - \frac{T_{acq}}{2})/T_2^*} \sum_{n=1}^{\infty} e^{-2n(\tau + T_{acq})/T_2^*} \ . \tag{C1}$$

Letting $x = \exp[-2\,(\tau + T_{acq}) / T_2^*]$, and recalling that the result for the convergent power series is

$\sum_{n=1}^{\infty} x^n = \frac{x}{1-x}$, the above expression becomes

$$e^{-2(\Delta - \tau - \frac{T_{acq}}{2})/T_2^*} \sum_{n=1}^{\infty} e^{-2n(\tau + T_{acq})/T_2^*} = e^{-2(\Delta - \tau - \frac{T_{acq}}{2})/T_2^*} \frac{e^{-2(\tau + T_{acq})/T_2^*}}{1 - e^{-2(\tau + T_{acq})/T_2^*}} = \frac{e^{-2\Delta/T_2^*} e^{-T_{acq}/T_2^*}}{1 - e^{-2(\tau + T_{acq})/T_2^*}}. \tag{C2}$$

Substituting this result into Eq. (3) yields Eq. (4). Note that the convergence criterion $|x| = \left|\exp[-2(\tau + T_{acq}) / T_2^*]\right| < 1$ is satisfied.

APPENDIX D

The propagation of noise from two FLASH images at α_1 and α_2 into the final T_1 map has been extensively studied (28), (29), and the T_1 standard deviation σ_{T1}, is related to the noise standard deviation σ_S, by (25)

$$\begin{aligned} \sigma_{\mathrm{T1}} &= \frac{T_1^2}{TR}\frac{\sin\alpha_1 \sin\alpha_2 \left|\cos\alpha_1 - \cos\alpha_2\right|\sqrt{S_1^2+S_2^2}}{A_1 A_2}\sigma_S\ , \\ A_1 &= \left[S_2 \sin\alpha_1 \cos\alpha_2 - S_1 \sin\alpha_2 \cos\alpha_1\right], \\ A_2 &= \left[S_2 \sin\alpha_1 - S_1 \sin\alpha_2\right]. \end{aligned} \qquad \text{(D1)}$$

In MPM with VFA-FLASH, Eq. (D1) also depends on T_2^*, because the MERGE combinations (S_{ME}) at each respective flip angle (α_i) may be written as G_{SNR} (Eq. (2)) multiplied by the FLASH signal at TE=0 ($S_{0,i}$),

$$S_i = S_{0,i}\sqrt{\sum_{n=1}^{N} e^{-2TE_n/T_2^*}}\ . \qquad \text{(D2)}$$

Therefore σ_{T1} in Eq. (D1) becomes reduced by a factor of G_{SNR}. Likewise, the noise standard deviation σ_{PD} of the proton density map PD derived by Sabati and Maudsley (30) can be modified straightforwardly to incorporate the G_{SNR} term, yielding

$$\begin{aligned} \sigma_{PD} &= \frac{\sigma_S\ PD}{G_{SNR}}\frac{\sqrt{A_1^2 S_{0,2}^4 + A_2^2 S_{0,1}^4}}{S_{0,1}S_{0,2}\left|A_1 S_{0,2} - A_2 S_{0,1}\right|}, \\ A_1 &= \tan\alpha_1 \sin\alpha_1(\sin\alpha_2 - \tan\alpha_2), \\ A_2 &= \tan\alpha_2 \sin\alpha_2(\sin\alpha_1 - \tan\alpha_1). \end{aligned} \qquad \text{(D3)}$$

Thus the SNR of the PD map also increases by a factor of G_{SNR} (Eq. (2)).

APPENDIX E

<u>Optimal weights for the combined T_2^*</u>

The variance of T_2^* can be calculated from the expression for the variance of R_2 derived by De Deene et al for a mono-exponential fit (Eq. 9 in (64)) by replacing R_2 with R_2^* and recalling that the relative error of inverses is identical ($\sigma_{R2*}/R_2^* = \sigma_{T2*}/T_2^*$), yielding

$$\sigma_{\mathrm{T2*}} \approx \frac{T_2^{*2}\sigma_S}{S_0}\frac{6e^{R_2^* TE_1}}{N(N^2-1)\Delta TE}\Gamma . \qquad \text{(E1)}$$

Here, N is the number of echoes, ΔTE is the echo spacing, TE_1 is the first echo time, S_0/σ_S is the SNR extrapolated to $TE=0$, and Γ is a function that is independent of the flip angle. Since in this expression only S_0 depends on the flip angle, we have $1/\sigma_{\mathrm{T2*}}^2 \propto S_0^2$. Since

$$S_{0,i} = PD\frac{(1-E_1)\sin(\alpha_i)}{1-E_1\cos(\alpha_i)}, \qquad \text{(E2)}$$

the weights of Eq. (12) simplify to

$$w_i = \frac{\sin^2(\alpha_i)}{(1-E_1\cos(\alpha_i))^2} . \qquad \text{(E3)}$$

ACKNOWLEDGMENTS

We gratefully acknowledge financial support from the Alberta Cancer Foundation, the Alberta Cancer Research Institute, and the Natural Sciences and Engineering Research Council (Canada). We also thank Philips Healthcare for technical support, Dr. Roger Luechinger for the PATI program used for data transfer, and the anonymous referees for insightful comments.

REFERENCES

1. Helms G, Dechent P. Increased SNR and reduced distortions by averaging multiple gradient echo signals in 3D FLASH imaging of the human brain at 3T. J. Magn. Reson. Imaging 2009;29:198–204.

2. Baldwin LN, Wachowicz K, Thomas SD, Rivest R, Fallone BG. Characterization, prediction, and correction of geometric distortion in 3 T MR images. Med. Phys. 2007;34:388.

3. Stanescu T, Jans H-S, Pervez N, Stavrev P, Fallone BG. A study on the magnetic resonance imaging (MRI)-based radiation treatment planning of intracranial lesions. Phys. Med. Biol. 2008;53:3579–93.

4. Lin F-H, Kwong KK, Belliveau JW, Wald LL. Parallel imaging reconstruction using automatic regularization. Magn. Reson. Med. 2004;51:559–67.

5. Haase A, Frahm J, Matthaei D, Hanicke W, Merboldt KD. FLASH imaging. Rapid NMR imaging using low flip-angle pulses. J. Magn. Reson. 1986;67:258–266.

6. Mugler JP, Brookeman JR. Three-dimensional magnetization-prepared rapid gradient-echo imaging (3D MP RAGE). Magn. Reson. Med. 1990;15:152–7.

7. Fischl B, Salat DH, Van der Kouwe AJW, Makris N, Ségonne F, Quinn BT, Dale AM. Sequence-independent segmentation of magnetic resonance images. Neuroimage 2004;23 Suppl 1:S69–84.

8. Van Der Kouwe AJW, Benner T, Salat DH, Fischl B. Brain morphometry with multiecho MPRAGE. Neuroimage 2008;40:559–69.

9. Wang HZ, Riederer SJ, Lee JN. Optimizing the precision in T1 relaxation estimation using limited flip angles. Magn. Reson. Med. 1987;5:399–416.

10. Lin W, Paczynski RP, Venkatesan R, He YY, Powers WJ, Hsu CY, Haacke EM. Quantitative regional brain water measurement with magnetic resonance imaging in a focal ischemia model. Magn. Reson. Med. 1997;38:303–310.

11. Venkatesan R, Lin W, Haacke EM. Accurate determination of spin-density and T1 in the presence of RF- field inhomogeneities and flip-angle miscalibration. Magn. Reson. Med. 1998;40:592–602.

12. Weiskopf N, Suckling J, Williams G, Correia MM, Inkster B, Tait R, Ooi C, Bullmore ET, Lutti A. Quantitative multi-parameter mapping of R1, PD*, MT, and R2* at 3T: A multi-center validation. Front. Neurosci. 2013;7:1–11.

13. Deoni SCL, Rutt BK, Peters TM. Synthetic T1-weighted brain image generation with incorporated coil intensity correction using DESPOT1. Magn. Reson. Imaging 2006;24:1241–8.

14. Nöth U, Hattingen E, Bähr O, Tichy J, Deichmann R. Improved visibility of brain tumors in synthetic MP-RAGE anatomies with pure T1 weighting. NMR Biomed. 2015;28:818–830.

15. Marques JP, Kober T, Krueger G, Van der Zwaag W, Van de Moortele P-F, Gruetter R. MP2RAGE, a self bias-field corrected sequence for improved segmentation and T1-mapping at high field. Neuroimage 2010;49:1271–81.

16. Metere R, Moller EH, Kruger G, Kober T, Schafer A. Simultaneous Quantitative Mapping of T1 , T2*, and Magnetic Susceptibility with Multi-Echo MP2RAGE at 7 T. In: International Society of Magnetic Resonance in Medicine. Vol. 23. ; 2015. p. 439.

17. Ocali O, Atalar E. Ultimate intrinsic signal-to-noise ratio in MRI. Magn. Reson. Med. 1998;39:462–73.

18. Vinitski S, Griffey R, Fuka M, Matwiyoff N, Prost R. Effect of the sampling rate on magnetic resonance imaging. Magn. Reson. Med. 1987;5:278–85.

19. Fleysher L, Fleysher R, Liu S, Zaaraoui W, Gonen O. Optimizing the precision-per-unit-time of quantitative MR metrics: examples for T1, T2, and DTI. Magn. Reson. Med. 2007;57:380–7.

20. Rahmer J, Börnert P, Groen J, Bos C. Three-dimensional radial ultrashort echo-time imaging with T2 adapted sampling. Magn. Reson. Med. 2006;55:1075–82.

21. Cardenas-Blanco A, Tejos C, Irarrazaval P, Cameron I. Noise in Magnitude Magnetic Resonance Images. Concepts Magn. Reson. Part A 2008;32A:409–416.

22. Bernstein MA, King KF, Zhou XJ. Handbook of MRI Pulse Sequences. Burlington: Elsevier Academic Press; 2004.

23. Deichmann R, Good CD, Josephs O, Ashburner J, Turner R. Optimization of 3-D MP-RAGE sequences for structural brain imaging. Neuroimage 2000;12:112–27.

24. Deoni SCL, Peters TM, Rutt BK. High-resolution T1 and T2 mapping of the brain in a clinically acceptable time with DESPOT1 and DESPOT2. Magn. Reson. Med. 2005;53:237–41.

25. Preibisch C, Deichmann R. T1 mapping using spoiled FLASH-EPI hybrid sequences and varying flip angles. Magn. Reson. Med. 2009;62:240–6.

26. Cheng H-LM, Wright GA. Rapid high-resolution T1 mapping by variable flip angles: accurate and precise measurements in the presence of radiofrequency field inhomogeneity. Magn. Reson. Med. 2006;55:566–74.

27. Manuel A, Li W, Jellus V, Hughes T, Prasad P V. Variable flip angle-based fast three-dimensional T1 mapping for delayed gadolinium-enhanced MRI of cartilage of the knee: need for B1 correction. Magn. Reson. Med. 2011;65:1377–83.

28. Deoni SCL, Rutt BK, Peters TM. Rapid combined T1 and T2 mapping using gradient recalled acquisition in the steady state. Magn. Reson. Med. 2003;49:515–26.

29. Schabel MC, Morrell GR. Uncertainty in T1 mapping using the variable flip angle method with two flip angles. Phys. Med. Biol. 2009;54:N1–8.

30. Sabati M, Maudsley AA. Fast and high-resolution quantitative mapping of tissue water content with full brain coverage for clinically-driven studies. Magn. Reson. Imaging 2013;31:1752–9.

31. Yarnykh VL. Actual flip-angle imaging in the pulsed steady state: a method for rapid three-dimensional mapping of the transmitted radiofrequency field. Magn. Reson. Med. 2007;57:192–200.

32. Roemer PB, Edelstein WA, Hayes CE, Souza SP, Mueller OM. The NMR phased array. Magn. Reson. Med. 1990;16:192–225.

33. Weiskopf N, Lutti A, Helms G, Novak M, Ashburner J, Hutton C. Unified segmentation based correction of R1 brain maps for RF transmit field inhomogeneities (UNICORT). Neuroimage 2011;54:2116–24.

34. Volz S, Nöth U, Deichmann R. Correction of systematic errors in quantitative proton density mapping. Magn. Reson. Med. 2012;68:74–85.

35. Tustison NJ, Avants BB, Cook PA, Zheng Y, Egan A, Yushkevich PA, Gee JC. N4ITK: improved N3 bias correction. IEEE Trans. Med. Imaging 2010;29:1310–20.

36. Bankman IN. Handbook of medical image processing and analysis. 2nd ed. Amsterdam: Elsevier Academic Press; 2009.

37. Perona P, Malik J. Scale-space and edge detection using anisotropic diffusion. IEEE Trans.

Pattern Anal. Mach. Intell. 1990;12:629–639.

38. Weiskopf N, Callaghan MF, Josephs O, Lutti A, Mohammadi S. Estimating the apparent transverse relaxation time (R2*) from images with different contrasts (ESTATICS) reduces motion artifacts. Front. Neurosci. 2014;8:1–10.

39. Wang H, Balter J, Cao Y. Patient-induced susceptibility effect on geometric distortion of clinical brain MRI for radiation treatment planning on a 3T scanner. Phys. Med. Biol. 2013;58:465–77.

40. Howarth C, Hutton C, Deichmann R. Improvement of the image quality of T1-weighted anatomical brain scans. Neuroimage 2006;29:930–7.

41. Lin C, Bernstein MA. 3D magnetization prepared elliptical centric fast gradient echo imaging. Magn. Reson. Med. 2008;59:434–9.

42. Christoffersson JO, Olsson LE, Sjöberg S. Nickel-doped agarose gel phantoms in MR imaging. Acta Radiol. 1991;32:426–31.

43. Nekolla S, Gneiting T, Syha J, Deichmann R, Haase A. T1 maps by K-space reduced snapshot-FLASH MRI. J. Comput. Assist. Tomogr. 1992;16:327–32.

44. Kato H, Yoshimura K, Kuroda M, et al. Development of a phantom compatible for MRI and hyperthermia using carrageenan gel-relationship between T1 and T2 values and NaCl concentration. Int. J. Hyperthermia 2004;20:803–814.

45. Fedorov A, Beichel R, Kalpathy-Cramer J, et al. 3D Slicer as an image computing platform for the Quantitative Imaging Network. Magn. Reson. Imaging 2012;30:1323–41.

46. Boyes RG, Gunter JL, Frost C, et al. Intensity non-uniformity correction using N3 on 3-T scanners with multichannel phased array coils. Neuroimage 2008;39:1752–62

47. Ahmed MN, Yamany SM, Mohamed N, Farag AA, Moriarty T. A modified fuzzy C-means algorithm for bias field estimation and segmentation of MRI data. IEEE Trans. Med. Imaging 2002;21:193–199.

48. Volz S, Nöth U, Jurcoane A, Ziemann U, Hattingen E, Deichmann R. Quantitative proton density mapping: correcting the receiver sensitivity bias via pseudo proton densities. Neuroimage 2012;63:540–52.

49. Neeb H, Zilles K, Shah NJ. A new method for fast quantitative mapping of absolute water content in vivo. Neuroimage 2006;31:1156–68.

50. Li J, Chang S, Liu T, Jiang H, Dong F, Pei M, Wang Q, Wang Y. Phase-corrected bipolar gradients in multi-echo gradient-echo sequences for quantitative susceptibility mapping. Magn. Reson. Mater. Physics, Biol. Med. 2015;28:347–355.

51. Hwang D, Kim D-H, Du YP. In vivo multi-slice mapping of myelin water content using T2* decay. Neuroimage 2010;52:198–204.

52. Oros-Peusquens AM, Laurila M, Shah NJ. Magnetic field dependence of the distribution of NMR relaxation times in the living human brain. MAGMA 2008;21:131–47.

53. Gelman N, Ewing JR, Gorell JM, Spickler EM, Solomon EG. Interregional variation of

longitudinal relaxation rates in human brain at 3.0 T: Relation to estimated iron and water contents. Magn. Reson. Med. 2001;45:71–79.

54. Wansapura JP, Holland SK, Dunn RS, Ball WS. NMR relaxation times in the human brain at 3.0 tesla. J. Magn. Reson. Imaging 1999;9:531–8.

55. Helms G, Dathe H, Dechent P. Quantitative FLASH MRI at 3T using a rational approximation of the Ernst equation. Magn. Reson. Med. 2008;59:667–72.

56. Neeb H, Ermer V, Stocker T, Shah NJ. Fast quantitative mapping of absolute water content with full brain coverage. Neuroimage 2008;42:1094–1109.

57. Abbas Z, Gras V, Möllenhoff K, Oros-Peusquens A-M, Shah NJ. Quantitative water content mapping at clinically relevant field strengths: A comparative study at 1.5T and 3T. Neuroimage 2015;106:404–13.

58. Langkammer C, Liu T, Khalil M, Enzinger C, Jehna M, Fuchs S, Fazekas F, Wang Y, Ropele S. Quantitative susceptibility mapping in multiple sclerosis. Radiology 2013;267:551–9.

59. Rioux JA, Levesque IR, Rutt BK. Biexponential longitudinal relaxation in white matter: Characterization and impact on T1 mapping with IR-FSE and MP2RAGE. Magn. Reson. Med. 2016;75:2265-2277.

60. Okubo G, Okada T, Yamamoto A, Kanagaki M, Fushimi Y, Okada T, Murata K, Togashi K. MP2RAGE for deep gray matter measurement of the brain: A comparative study with MPRAGE. J. Magn. Reson. Imaging 2016;43:55–62.

61. Diakova G, Korb J-P, Bryant RG. The magnetic field dependence of water T1 in tissues. Magn. Reson. Med. 2012;68:272–7.

62. Keil B, Wald LL. Massively parallel MRI detector arrays. J. Magn. Reson. 2013;229:75–89.

63. Taylor JR. An introduction to error analysis. 2nd ed. Sausalito: University Science Books; 1997.

64. Deene YD, Walle RV De, Achten E, Wagter CD. Mathematical analysis and experimental investigation of noise in quantitative magnetic resonance imaging applied in polymer gel dosimetry. Signal Processing 1998;70:85–101.

FIGURE CAPTIONS

Figure 1: (a) Relative SNR as a function of the acquisition time, T_{acq}, for a single echo (Eq. (1), red curves) and SNR for a Multi-Echo Recombined Gradient Echo image (MERGE, Eq. (4)) with 9 echoes (Eq. (3), green curves) and an infinite number of echoes (black curves) at T_2^*= (100, 50, 25, 10 and 5 ms), with dead times Δ=1.3 ms, and τ=0.4 ms. Both Vinitski's and Fleysher's expressions are plotted for comparison. (b) SNR efficiency ($\propto SNR/\sqrt{TR}$) as a function of TR for a bipolar multi-echo FLASH sequence (black) and single-echo FLASH (green) normalized to that of a typical single-echo FLASH with TR=8 ms, T_{acq}=5.7 ms (as long as possible), and T_1=1200 ms. The bipolar echo sequence has a fixed T_{acq}=1.93 ms, and enough echoes to fill the TR. Flip angles are equal to the Ernst angle. Dead times are the same as in (a), with an additional spoiler gradient duration of 1 ms.

Figure 2: Multi-parameter mapping pipeline for (a) VFA-FLASH and (b) MP2RAGE. Note that the mean flip angle over the brain (excluding air cavities), $\langle c_{RF} \rangle$, is needed to convert the bias field Ψ_{T1} into the correct c_{RF}^+ map. The post-processing steps after N4ITK are shown as dashed arrows for clarity. See the Methods section for further details.

Figure 3: a) Measured SNR in 5 agar phantom layers using single-echo and multi-echo FLASH and MPRAGE sequences. (b) Measured and predicted SNR gains for the multi-echo FLASH and MPRAGE with respect to their single-echo counterparts. (c) Measured T_1NR with the different MPM protocols. (d) Measured and predicted T_1NR gains of the multi-echo MPM protocols with respect to their single-echo counterparts. (e) Measured PDNR with the different MPM protocols. (f) Measured T_2^*NR with the different multi-echo MPM protocols. Error bars correspond to the standard deviation from 5 SNR measurements in each layer (an estimate of SNR uniformity).

Figure 4: Phantom sagittal PD, T_1 and T_2^* maps derived from the various MP2RAGE and VFA-FLASH protocols, as well as an example of the bias field Ψ_{PD} corresponding to MP2R1, and the c_{RF} corresponding to VFA-FLASH1. The green arrows point to an overestimation in the proton density arising from susceptibility effects at the phantom edges.

Figure 5: Axial T_1, PD and T_2^* maps of the first volunteer (v1) derived from the four MPM protocols (~8:30 min each) at the same slice location.

Figure 6: Sagittal parametric maps (PD, T_1 and T_2^*) of the 4 volunteers derived from the VFA-FLASH9 protocol. Susceptibility effects in the frontal sinuses tend to result in an overestimation of the proton density at the bottom surface of the frontal lobe (red arrows).

Figure 7: (a-c) Normalized T_1, *PD* and T_2^* histograms of volunteer v1 derived from all 6 MPM protocols, and **(d-f)** normalized T_1, *PD* and T_2^* histograms of the four volunteers for the VFA-FLASH9 protocol.

Figure 8: Normalized T_1 histograms of volunteer v1 derived from each separate echo of (a) the MP2R6 protocol, and (b) the VFA-FLASH6 protocol. .

TABLES

Protocol Name	**α_1/α_2 (°)**	***N***	**$TE_1/\Delta TE/TR/TI_1/TI_2$ (ms)**	**BW (Hz/ pix)**	**SENSE factor AP × RL**	**TFE / TR_{MP} (ms)**	**Scan dur. (min:s)**	**ε (%)**
	MPRAGE Protocols							
MPR1	7/-	1	4.6/ - /8.8/1100/ -	175	1 × 1	240/3000	8:32	46
MPR6	9.5/-	6	2.3/2.3/16/1100/ -	517	2 × 1	123/3000	8:32	48
	FLASH Protocols							
FLASH1	22/-	1	4.6/ - /11/ - / -	175	1 × 1	-	5:56	52
FLASH8	31/-	8	2.3/2.3/22/ - / -	517	2 × 1	-	6:02	70
	MP2RAGE Protocols							
MP2R1	4/4	1	3.8/ - /8.0/750/2200	180	1.45 × 1.66	170/5000	8:40	36
MP2R6	6/6	6	2.3/2.3/16/750/2200	540	2.4 × 2	85/5000	8:40	38
	VFA-FLASH Protocols*							
VFA-FLASH1	3.5/20	1	4.6/ - /11/ - / -	175	1.2 × 1.2	-	8:46	52
VFA-FLASH6	4.5/25	6	2.3/2.3/16.5/ - / -	517	1.45 × 1.47	-	8:38	70
VFA-FLASH9	5.3/30	9	2.3/2.3/24/ - / -	517	1.75 × 1.77	-	8:33	73
VFA-FLASH12	6.0/34	12	2.3/2.3/31/ - / -	517	2 × 2	-	8:26	75

Table 1: MRI protocols with their relevant scan parameters optimized for a Philips 3T Achieva scanner. In all cases, the profile order was linear, non-selective RF excitation pulses were used, and the field-of-view (FOV) was 240 × 240 × 170 mm^3 with 1 mm isotropic resolution. *Note that both FLASH acquisitions (~4 min at α_1 and ~4 min at α_2) are counted as part of the total scan duration.

Protocol/ ROI Location	VFA-FLASH9			MP2R1		MP2R6		Reported Literature		
	PD *[%]*	T_1 *[ms]*	T_2^* *[ms]*	*PD* *[%]*	T_1 *[ms]*	*PD* *[%]*	T_1 *[ms]*	*PD* *[%]*	T_1 *[ms]*	T_2^* *[ms]*
Putamen L	82.3 (1.5)	1204 (22)	42.2 (4.4)	81.9 (2.5)	1207 (32)	83.4 (1.3)	1187 (33)	81.9[g], 83.2[h]	1337[a], 1140[b]	41.3[j]
Putamen R	82.5 (1.5)	1245 (49)	41.8 (6.0)	81.1 (1.5)	1212 (28)	84.8 (1.0)	1221 (35)	81.9[g], 83.2[h]	1321[a], 1140[b]	41.3[j]
Globus Pallidus L	77.0 (2.0)	962 (39)	28.6 (3.7)	75.3 (1.3)	916 (37)	78.6 (2.6)	931 (41)	76.8[i]	888[b], 1043[c]	26.7[j]
Globus Pallidus R	77.4 (1.1)	973 (38)	28.5 (3.3)	75.6 (1.4)	931 (34)	79.0 (0.5)	942 (34)	76.8[i]	888[b], 1043[c]	26.7[j]
Caudate L	84.8 (1.6)	1409 (46)	50.6 (4.9)	88.6 (2.5)	1345 (28)	85.2 (1.8)	1333 (10)	81.5[g], 84.8[h]	1524[a], 1464[e]	54.9[d] 47.4[j]
Caudate R	84.8 (1.7)	1372 (55)	52.3 (6.1)	88.4 (1.6)	1342 (11)	88.5 (1.5)	1403 (32)	81.5[g], 84.8[h]	1437[a], 1464[e]	54.9[d] 47.4[j]
Splenium	67.6 (0.6)	828 (41)	37.3 (0.4)	71.5 (1.2)	777 (15)	71.3 (0.9)	783 (18)	70.1[g], 66.2[h]	730[b], 773[f]	–
Genu	69.2 (1.5)	835 (66)	38.4 (1.6)	66.9 (1.6)	755 (24)	70.3 (0.9)	771 (27)	69.6[g], 69.0[h]	898[a], 720[b]	40[e],
Frontal WM L	69.1 (0.8)	854 (51)	43.1 (1.8)	66.0 (0.4)	807 (17)	69.1 (0.8)	798 (31)	70.1[g], 69.1[h]	947[a], 838[d]	44.7[d]
Frontal WM R	69.2 (0.8)	854 (45)	43.1 (1.8)	66.0 (0.9)	810 (18)	69.5 (1.5)	830 (16)	70.4[g], 69.1[h]	921[a], 847[c]	44.7[d]
Occipital WM L	69.5 (1.5)	838 (55)	44.1 (1.2)	66.6 (1.7)	811 (15)	71.0 (1.5)	832 (17)	69.0[g], 66.9[h]	954[a], 832[d]	48.4[d]
Occipital WM R	69.9 (1.3)	856 (50)	43.9 (1.4)	66.6 (1.3)	813 (17)	71.1 (0.8)	813 (22)	69.5[g], 66.9[h]	940[a], 832[d]	48.4[d]
Ventricle L	110 (2.8)	4424 (476)	145 (4.9)	127 (7.2)	2369 (57)	125 (2.7)	2345 (61)	99.9[i]	4306[f]	–
Ventricle R	110 (3.4)	4413 (478)	143 (4.3)	126 (3.0)	2378 (27)	126 (3.2)	2325 (51)	99.9[i]	4306[f]	–

Table 2: Measured *PD*, T_1 & T_2^* (with standard deviations) in various brain ROIs (in axial slices) averaged across 4 volunteers. Note that the T_2^* from MP2R6 was not measured because of its poor SNR and accuracy (Figure 5 or Figure 7c). Literature references are: [a] (25), [b] (52), [c] (53), [d] (54), [e] (12), [f] (55), [g] (34), [h] (56), [i] (57), [j] (58). Most authors average the left and right hemisphere measurements, except in (25), and (34). N.B.: *PD* is normalized with respect to the midpoint between WM and GM histogram peaks, and then multiplied by 76% (see text).

Online Supporting Information

Additional Supporting Information may be found in the online version of this article.

Supporting Figure S1: Measured PDNR in the multi-layered agar phantom for PD_1, PD_2 and PD_{wav}. The error bars correspond to the standard deviation of the 5 SNR measurements (ROIs) in each layer. As expected, the null point in PD_1 yields PDNR≈0 (middle layer, orange bar). ROI locations are the same as those in Supp. Fig. S4 below.

Supporting Figure S2: (a) SNR vs. the number of echoes (or TE_{max}) included in the MERGE combination (at the minimum T_{acq}=1.12 ms) for four different concentrations of $MnCl_2$-doped gelatin. The solid lines correspond to the SNR measured using the noise-scan method, the circles to the image-subtraction method, and the dots to the ROI-FFT method. The dashed curves are theoretical SNR extrapolations using Eq. (2) based on the T_2^* and the SNR of the first echo, showing excellent agreement with measurements. (b) SNR of the first echo (minimum TE) versus T_{acq} for the four different concentrations of $MnCl_2$-doped gelatin (dashed curves and filled circles/squares) and SNR of the MERGE image consisting of all 32 echoes combined (solid curves and empty circles/squares) for the same four $MnCl_2$-doped gelatin beakers.

Supporting Figure S3: Mean T_1NR (average of 5 ROIs per layer) in 5 different agar T_1 layers at 3T for the five MP2RAGE protocols proposed by J.P. Marques et al (for a 3T scanner), compared to the MP2R1 protocol re-optimized in this study (identical scan time of 8:30min per protocol). The MP2R1 protocol of this study slightly outperforms those proposed by Marques et al, most probably because of its lower bandwidth of ~180 Hz/pix. The acquisition bandwidth of all protocols was chosen as low as possible on our scanner. N.B.: Phantom T_1 values are different from Figure 3 because the MP2RAGE measurements were performed several weeks earlier.

Supporting Figure S4: Phantom sagittal images (arbitrary units) of conventional single-echo MPRAGE and FLASH, compared to the first echo (TE_1=2.3 ms) image and the MERGE combination of the corresponding multi-echo protocols. MPRAGE images are approximately corrected for flip angle inhomogeneity by dividing them by c_{RF}^2, while FLASH images are left uncorrected. ROI locations for all phantom measurements are displayed at the top.

Supporting Figure S5: Comparisons of the T_1 (a) and T_2^* (b) measurements within each agar layer of the multi-layered phantom. Note that (except for IR-EPI), the error bars correspond to the standard deviation of the 5 ROI measurements in each layer (yielding an estimate of the T_1 or T_2^* uniformity over the phantom).

Supporting Figure S6: Normalized T_1 and *PD* histograms from MP2R1 (a, c), and MP2R6 (b, d), for all four volunteers. Notice the smaller GM-WM peak separation of the histograms derived from MP2R6.

Supporting Figure S7: Effect of B_1^+ inhomogeneity (for a typical c_{RF}^+ range observed at 3T) on the T_1 look-up table of MP2R1 (dashed lines) and MP2R6 (solid lines). Note that, in practice, the table was made bijective by limiting the maximum T_1 to T_{1max}.

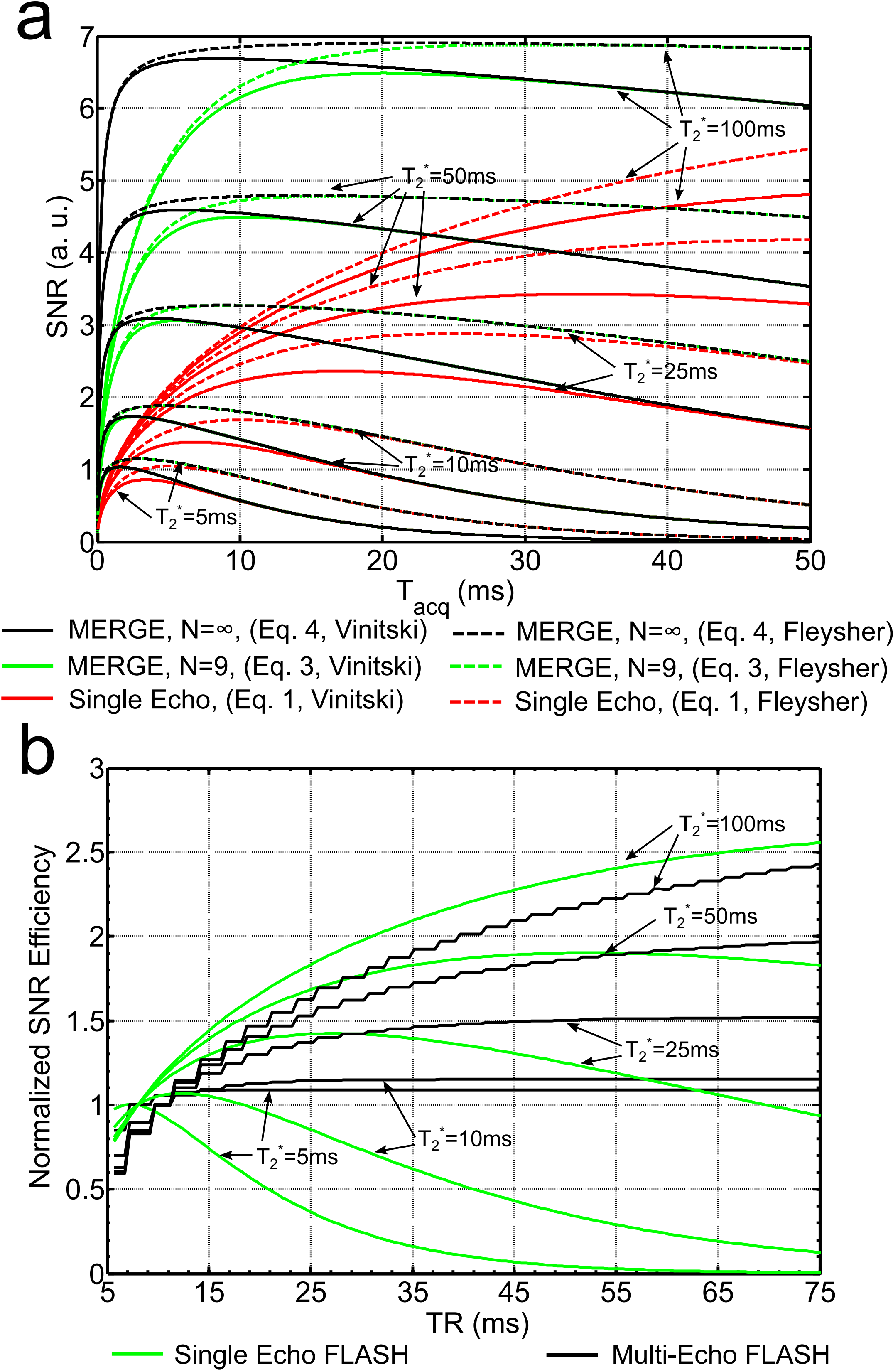
a
SNR (a. u.)
T_{acq} (ms)
T_2^*=100ms
T_2^*=50ms
T_2^*=25ms
T_2^*=10ms
T_2^*=5ms
MERGE, N=∞, (Eq. 4, Vinitski)
MERGE, N=9, (Eq. 3, Vinitski)
Single Echo, (Eq. 1, Vinitski)
MERGE, N=∞, (Eq. 4, Fleysher)
MERGE, N=9, (Eq. 3, Fleysher)
Single Echo, (Eq. 1, Fleysher)
b
Normalized SNR Efficiency
TR (ms)
T_2^*=100ms
T_2^*=50ms
T_2^*=25ms
T_2^*=10ms
T_2^*=5ms
Single Echo FLASH
Multi-Echo FLASH

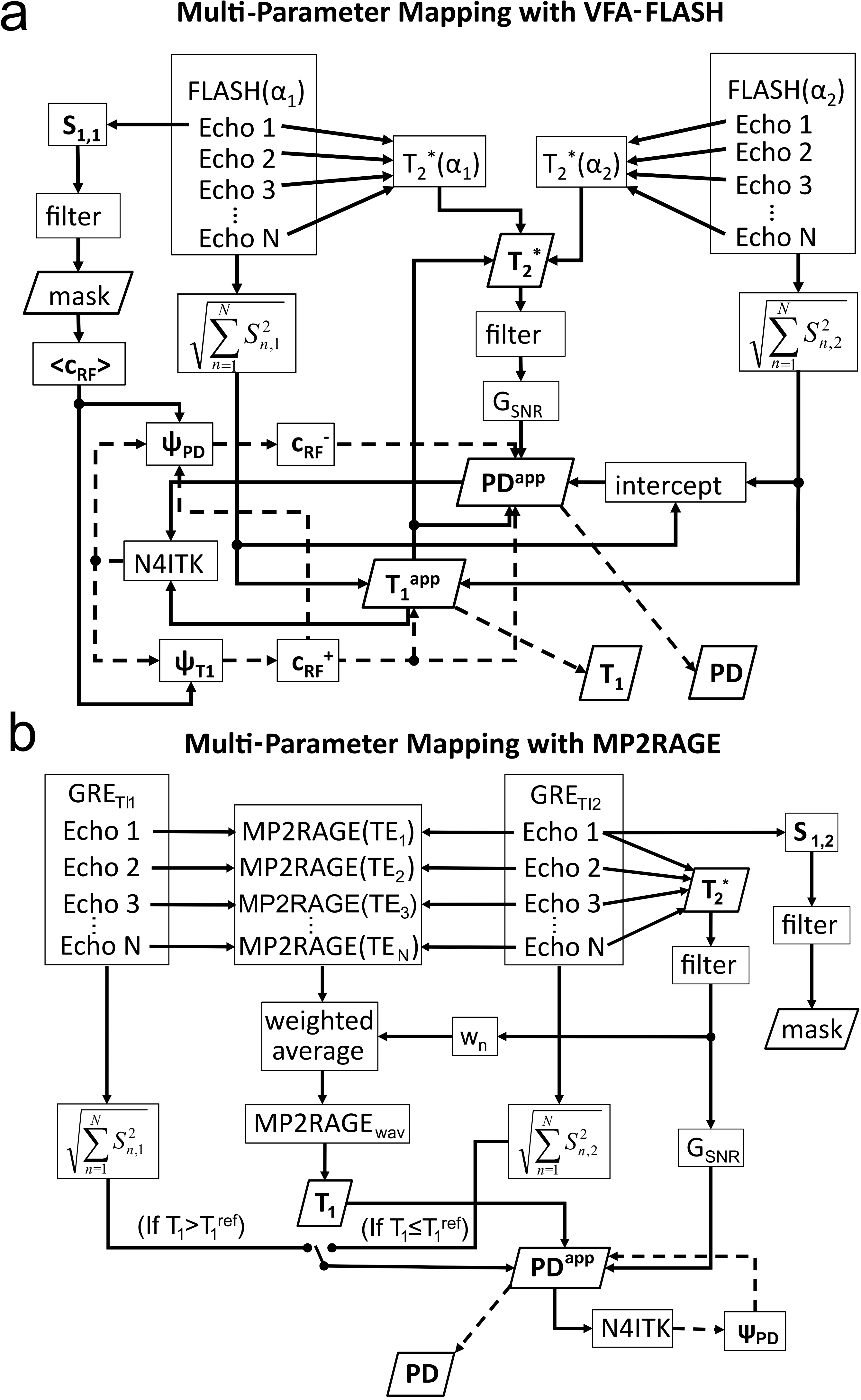

a
Multi-Parameter Mapping with VFA-FLASH
FLASH(α_1)
Echo 1
Echo 2
Echo 3
Echo N
FLASH(α_2)
Echo 1
Echo 2
Echo 3
Echo N
$S_{1,1}$
filter
mask
$<c_{RF}>$
$T_2^*(\alpha_1)$
$T_2^*(\alpha_2)$
T_2^*
filter
G_{SNR}
$\sqrt{\sum_{n=1}^{N} S_{n,1}^2}$
$\sqrt{\sum_{n=1}^{N} S_{n,2}^2}$
ψ_{PD}
c_{RF}^-
PD^{app}
intercept
N4ITK
T_1^{app}
ψ_{T1}
c_{RF}^+
T_1
PD
b
Multi-Parameter Mapping with MP2RAGE
GRE_{TI1}
Echo 1
Echo 2
Echo 3
Echo N
MP2RAGE(TE_1)
MP2RAGE(TE_2)
MP2RAGE(TE_3)
MP2RAGE(TE_N)
GRE_{TI2}
Echo 1
Echo 2
Echo 3
Echo N
$S_{1,2}$
filter
mask
T_2^*
filter
weighted average
w_n
G_{SNR}
$\sqrt{\sum_{n=1}^{N} S_{n,1}^2}$
$MP2RAGE_{wav}$
$\sqrt{\sum_{n=1}^{N} S_{n,2}^2}$
T_1
(If $T_1 > T_1^{ref}$)
(If $T_1 \leq T_1^{ref}$)
PD^{app}
N4ITK
ψ_{PD}
PD

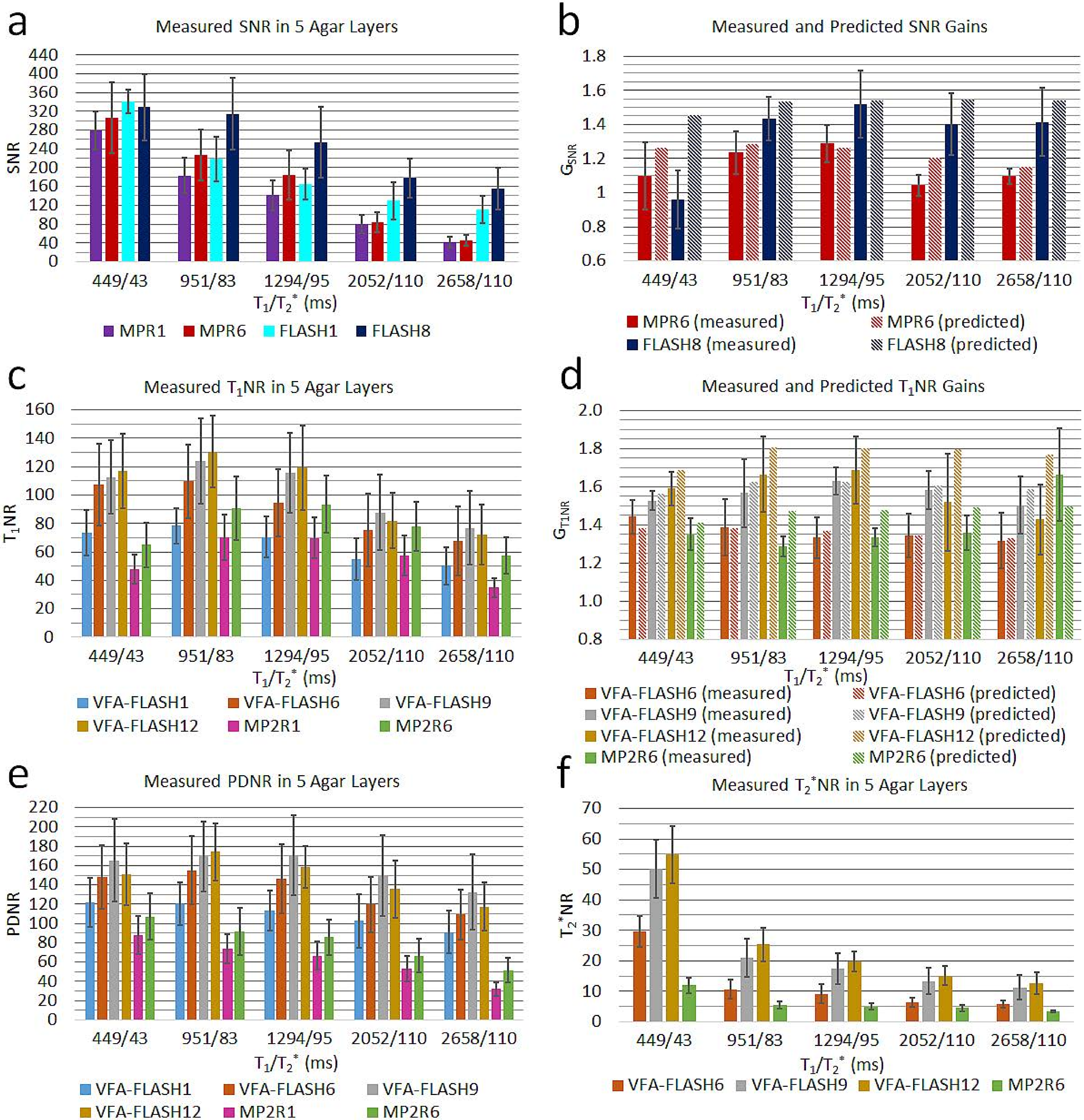
a
Measured SNR in 5 Agar Layers
SNR
440
400
360
320
280
240
200
160
120
80
40
0
449/43
951/83
1294/95
2052/110
2658/110
T1/T2* (ms)
MPR1
MPR6
FLASH1
FLASH8
b
Measured and Predicted SNR Gains
GSNR
1.8
1.6
1.4
1.2
1
0.8
0.6
449/43
951/83
1294/95
2052/110
2658/110
T1/T2* (ms)
MPR6 (measured)
MPR6 (predicted)
FLASH8 (measured)
FLASH8 (predicted)
c
Measured T1NR in 5 Agar Layers
T1NR
160
140
120
100
80
60
40
20
0
449/43
951/83
1294/95
2052/110
2658/110
T1/T2* (ms)
VFA-FLASH1
VFA-FLASH6
VFA-FLASH9
VFA-FLASH12
MP2R1
MP2R6
d
Measured and Predicted T1NR Gains
GT1NR
2.0
1.8
1.6
1.4
1.2
1.0
0.8
449/43
951/83
1294/95
2052/110
2658/110
T1/T2* (ms)
VFA-FLASH6 (measured)
VFA-FLASH6 (predicted)
VFA-FLASH9 (measured)
VFA-FLASH9 (predicted)
VFA-FLASH12 (measured)
VFA-FLASH12 (predicted)
MP2R6 (measured)
MP2R6 (predicted)
e
Measured PDNR in 5 Agar Layers
PDNR
220
200
180
160
140
120
100
80
60
40
20
0
449/43
951/83
1294/95
2052/110
2658/110
T1/T2* (ms)
VFA-FLASH1
VFA-FLASH6
VFA-FLASH9
VFA-FLASH12
MP2R1
MP2R6
f
Measured T2*NR in 5 Agar Layers
T2*NR
70
60
50
40
30
20
10
0
449/43
951/83
1294/95
2052/110
2658/110
T1/T2* (ms)
VFA-FLASH6
VFA-FLASH9
VFA-FLASH12
MP2R6

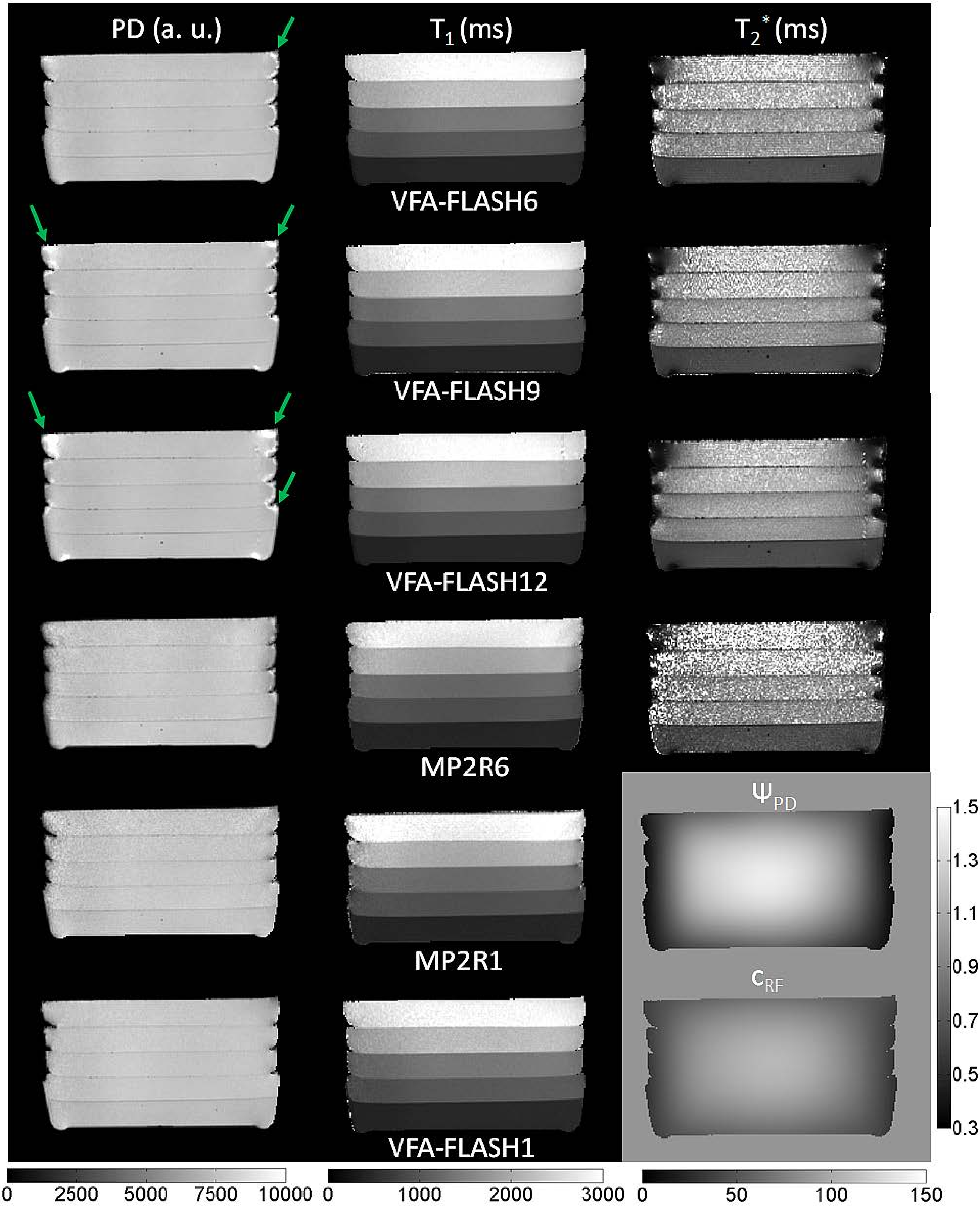
PD (a. u.)
T$_1$ (ms)
T$_2^*$ (ms)
VFA-FLASH6
VFA-FLASH9
VFA-FLASH12
MP2R6
MP2R1
VFA-FLASH1
Ψ$_{PD}$
c$_{RF}$
1.5
1.3
1.1
0.9
0.7
0.5
0.3
0
2500
5000
7500
10000
0
1000
2000
3000
0
50
100
150

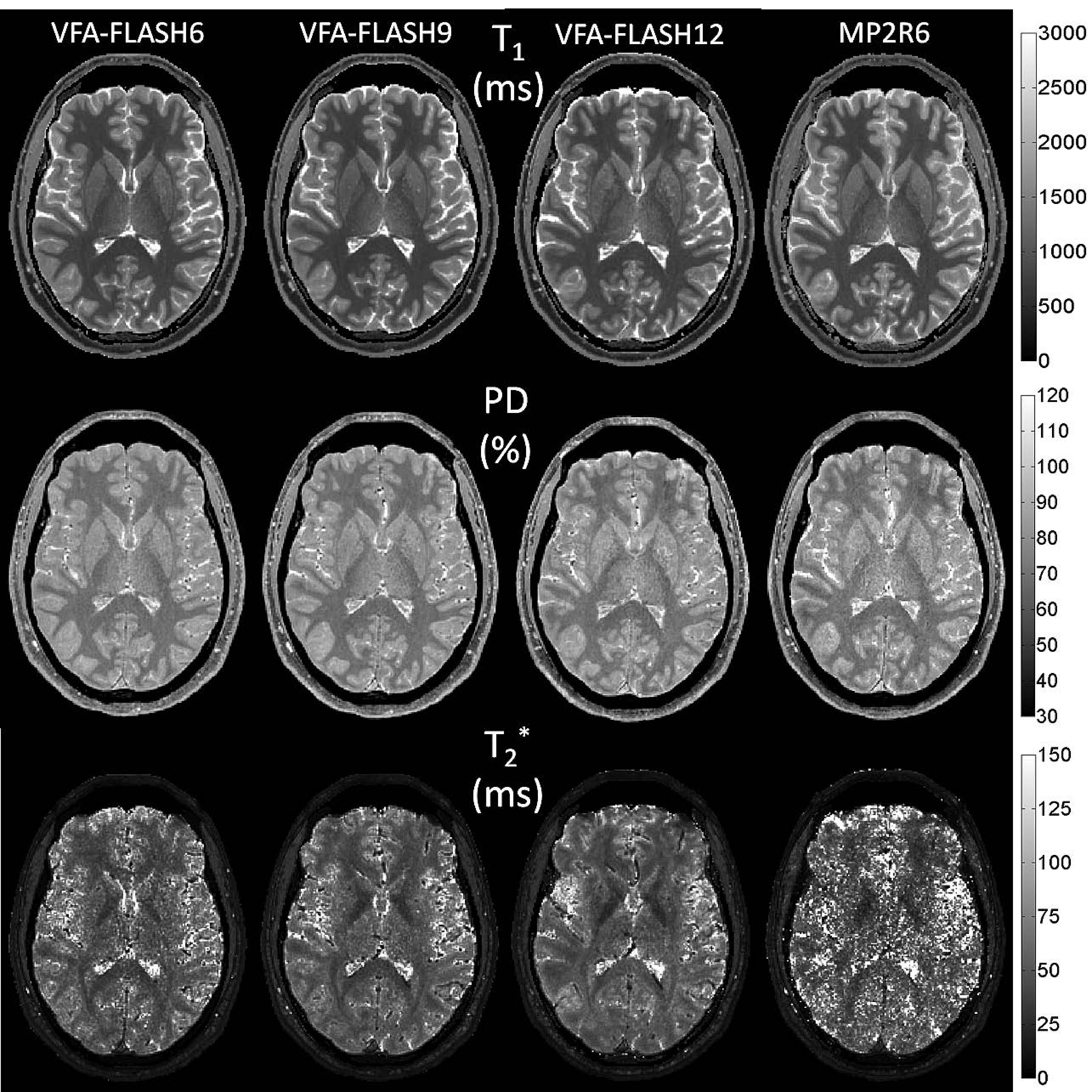
VFA-FLASH6
VFA-FLASH9
T_1 (ms)
VFA-FLASH12
MP2R6
3000
2500
2000
1500
1000
500
0
PD (%)
120
110
100
90
80
70
60
50
40
30
T_2^* (ms)
150
125
100
75
50
25
0

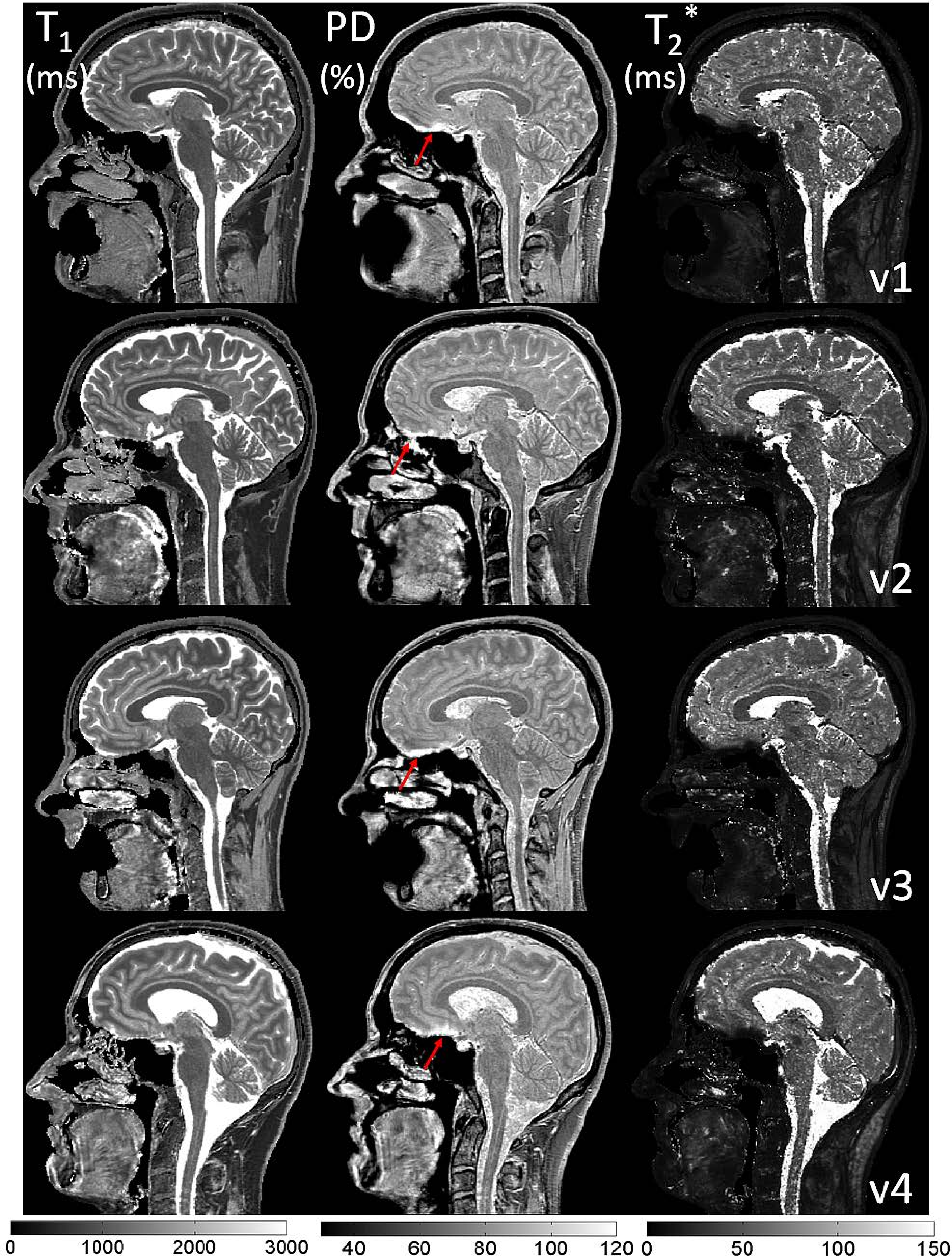

T1 (ms)
PD (%)
T2* (ms)
v1
v2
v3
v4
0
1000
2000
3000
40
60
80
100
120
0
50
100
150

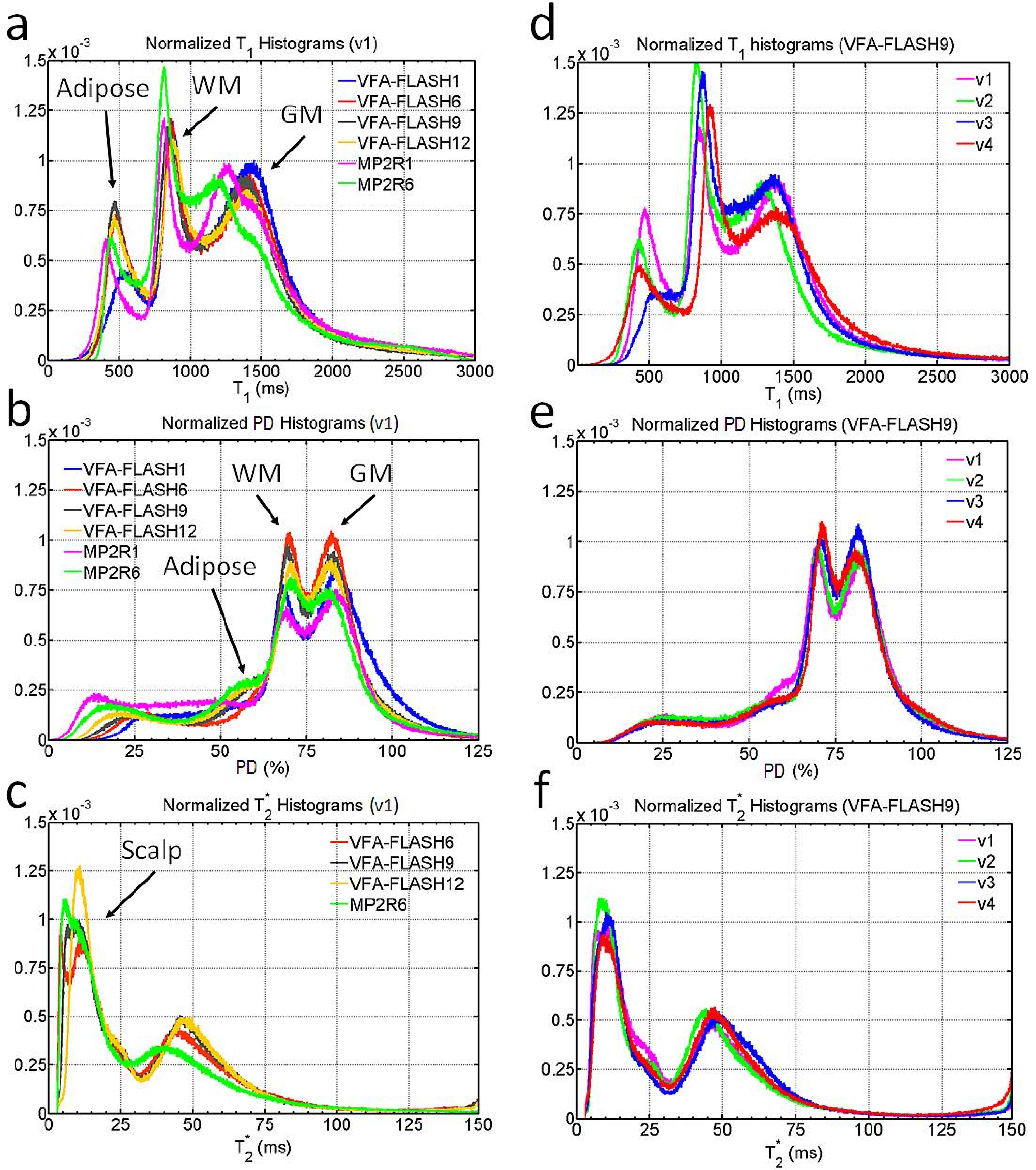
a
Normalized T1 Histograms (v1)
x 10-3
Adipose
WM
GM
VFA-FLASH1
VFA-FLASH6
VFA-FLASH9
VFA-FLASH12
MP2R1
MP2R6
T1 (ms)
b
Normalized PD Histograms (v1)
WM
GM
Adipose
PD (%)
c
Normalized T2* Histograms (v1)
Scalp
T2* (ms)
d
Normalized T1 histograms (VFA-FLASH9)
v1
v2
v3
v4
e
Normalized PD Histograms (VFA-FLASH9)
f
Normalized T2* Histograms (VFA-FLASH9)

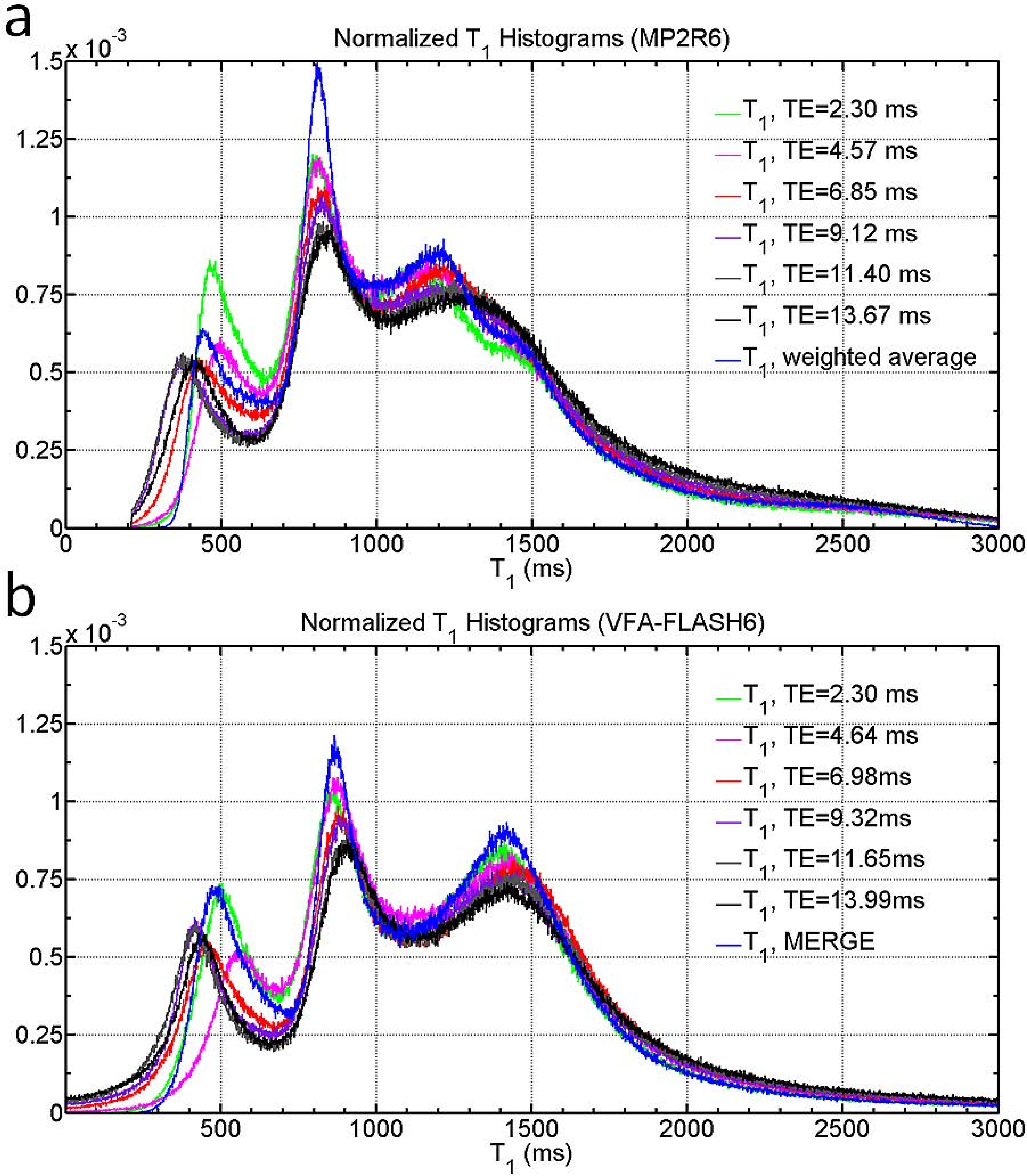
a
Normalized T1 Histograms (MP2R6)
x 10-3
1.5
1.25
1
0.75
0.5
0.25
0
0
500
1000
1500
2000
2500
3000
T1 (ms)
T1, TE=2.30 ms
T1, TE=4.57 ms
T1, TE=6.85 ms
T1, TE=9.12 ms
T1, TE=11.40 ms
T1, TE=13.67 ms
T1, weighted average
b
Normalized T1 Histograms (VFA-FLASH6)
x 10-3
1.5
1.25
1
0.75
0.5
0.25
0
500
1000
1500
2000
2500
3000
T1 (ms)
T1, TE=2.30 ms
T1, TE=4.64 ms
T1, TE=6.98ms
T1, TE=9.32ms
T1, TE=11.65ms
T1, TE=13.99ms
T1, MERGE

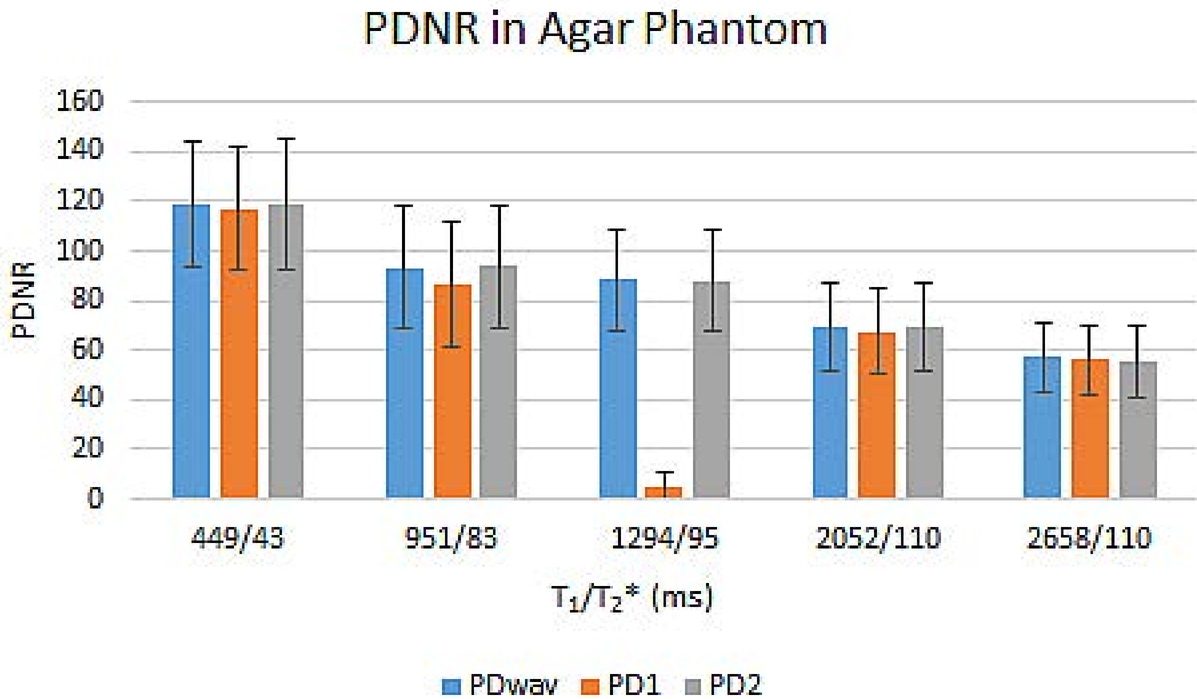

PDNR in Agar Phantom
PDNR
160
140
120
100
80
60
40
20
0
449/43
951/83
1294/95
2052/110
2658/110
T1/T2* (ms)
PDwav
PD1
PD2

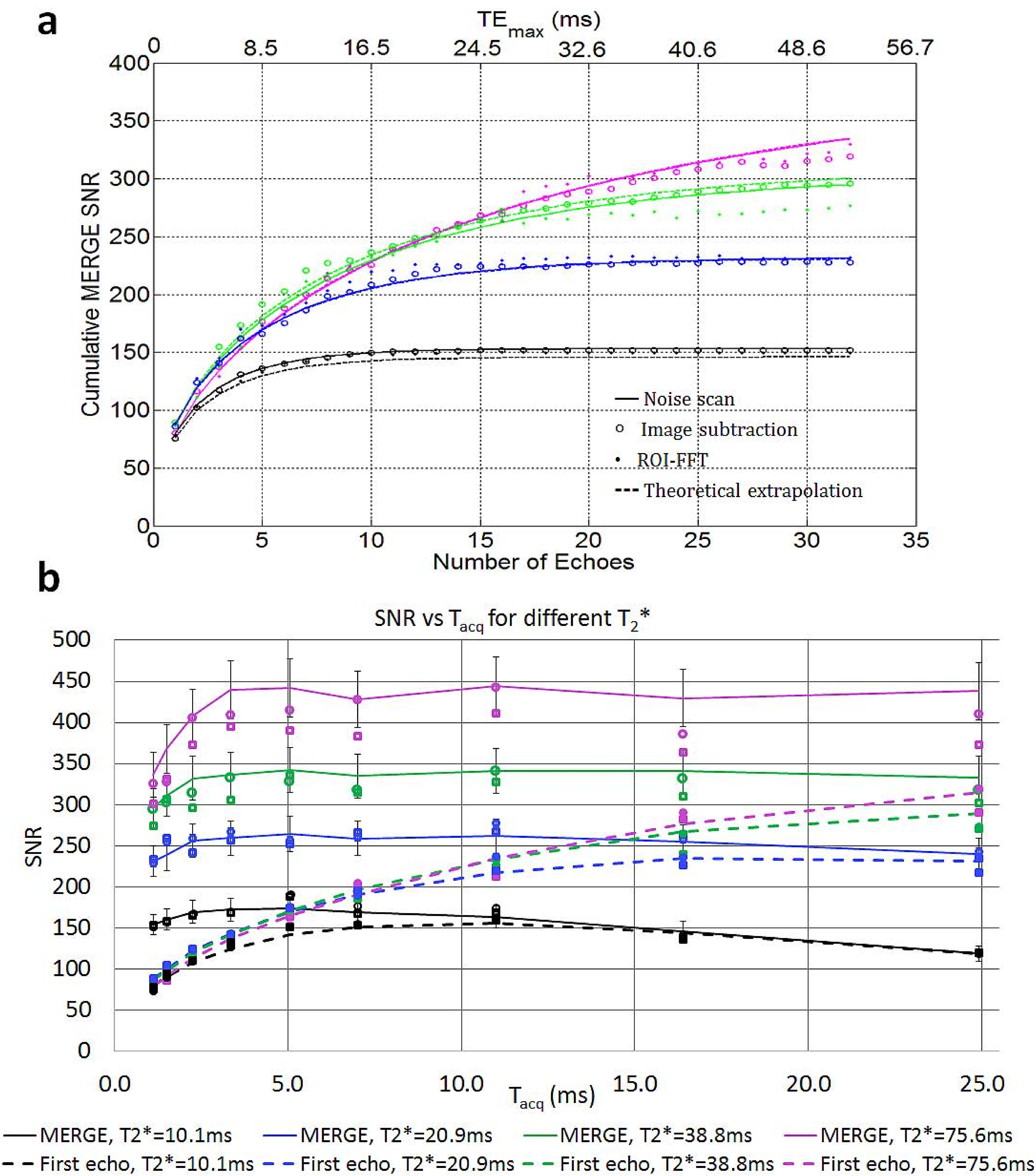
a
TE$_{max}$ (ms)
0
8.5
16.5
24.5
32.6
40.6
48.6
56.7
Cumulative MERGE SNR
Number of Echoes
Noise scan
Image subtraction
ROI-FFT
Theoretical extrapolation
b
SNR vs T$_{acq}$ for different T$_2$*
SNR
T$_{acq}$ (ms)
MERGE, T2*=10.1ms
MERGE, T2*=20.9ms
MERGE, T2*=38.8ms
MERGE, T2*=75.6ms
First echo, T2*=10.1ms
First echo, T2*=20.9ms
First echo, T2*=38.8ms
First echo, T2*=75.6ms

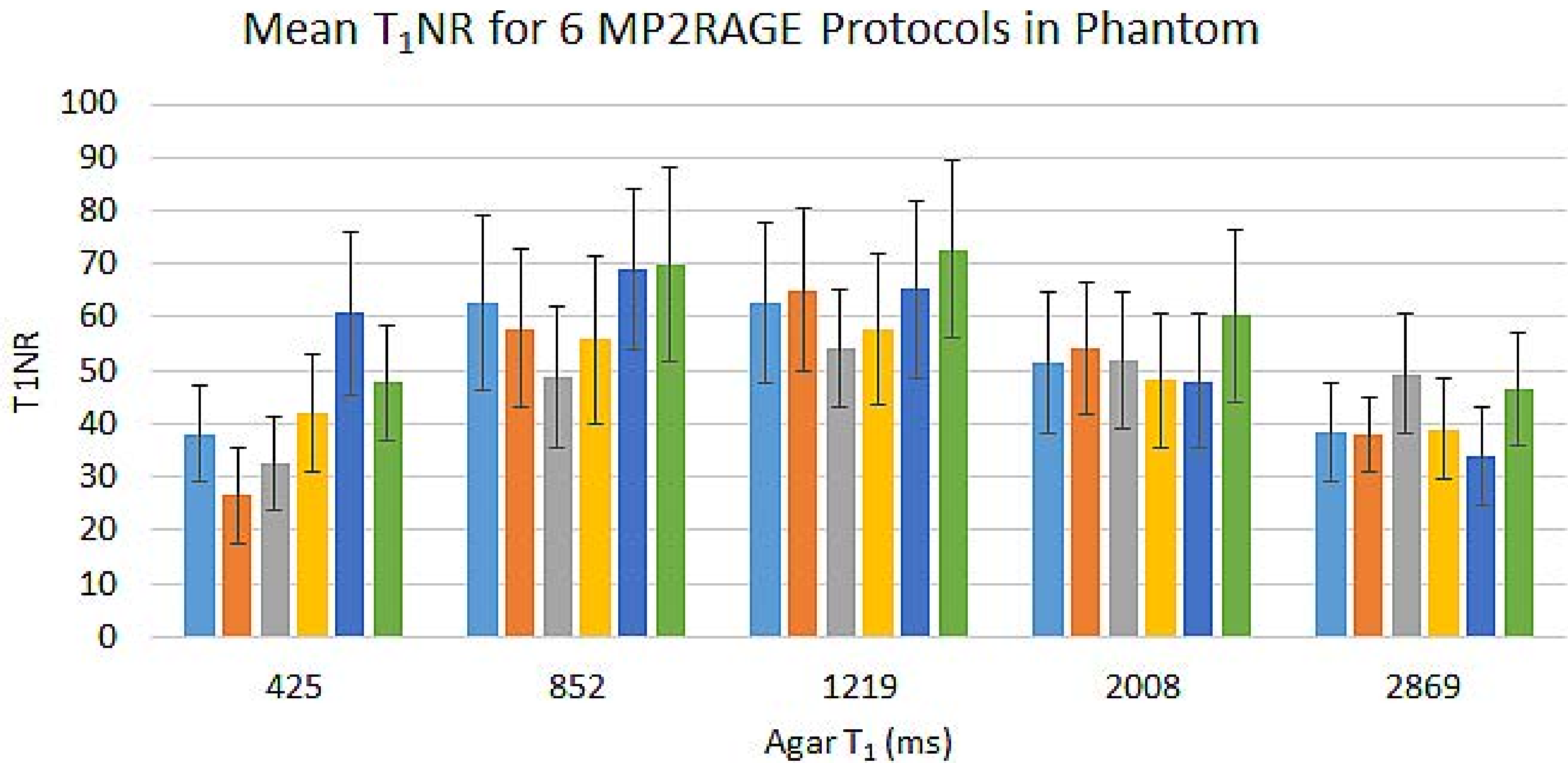

	JPM1	JPM2	JPM3	JPM4	JPM5	MP2R1 (this study)
TR_{MP}/TR (ms)	6750/7.9	6250/5.8	6250/5.8	5000/5.8	4000/5.8	5000/8.0
TI_1/TI_2 (ms)	800/3200	800/2200	800/2200	700/2000	600/1800	750/2200
α_1/α_2 (deg)	4/4	7/5	4/5	4/5	4/5	4/4
R (SENSE acc)	1.54x2.26	1.54x2.08	1.54x2.08	1.54x1.66	1.52x1.32	1.45x1.66
BW (Hz/pix)	189	293	293	293	293	178

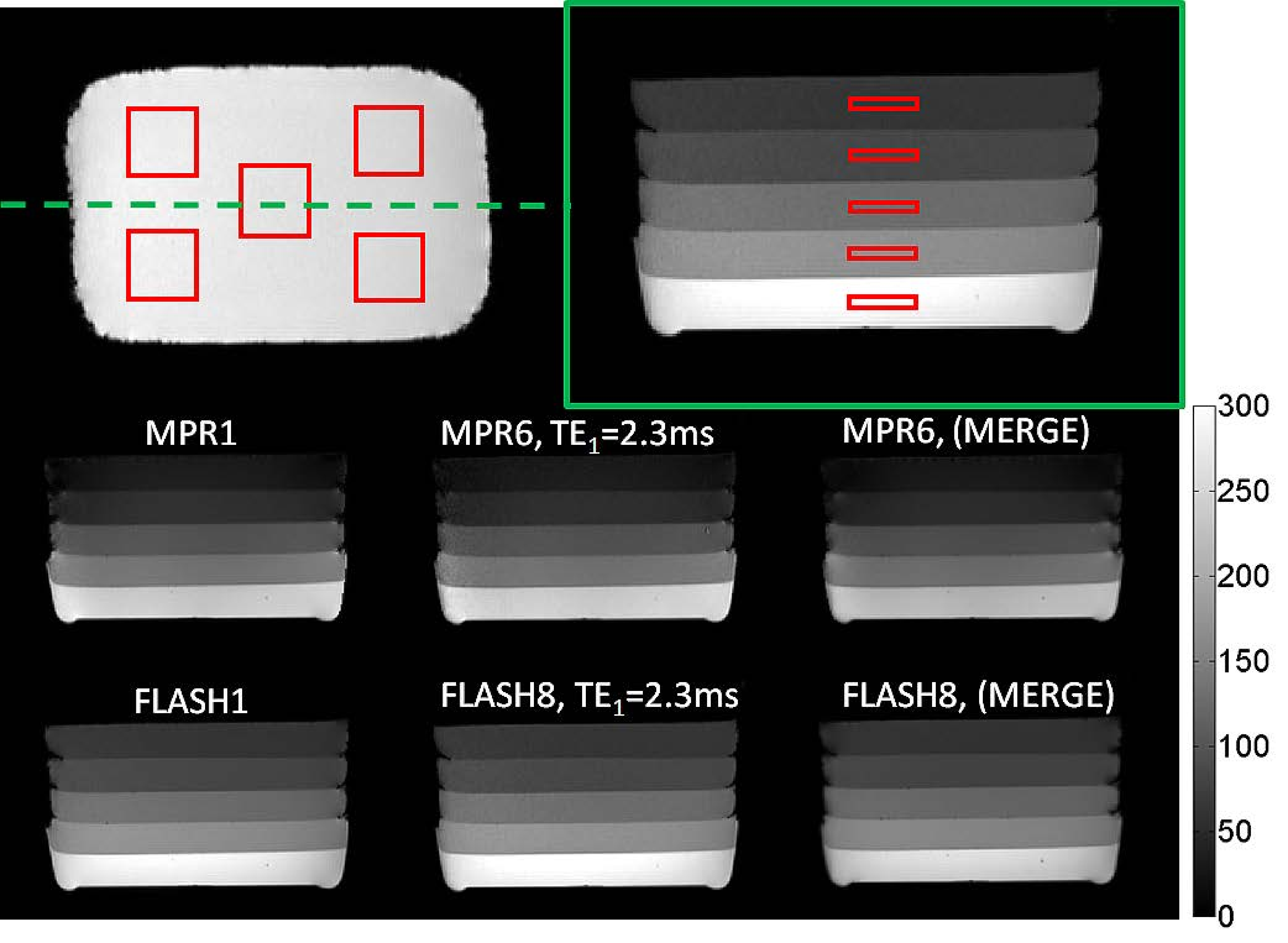

MPR1
MPR6, TE_1=2.3ms
MPR6, (MERGE)
FLASH1
FLASH8, TE_1=2.3ms
FLASH8, (MERGE)
300
250
200
150
100
50
0

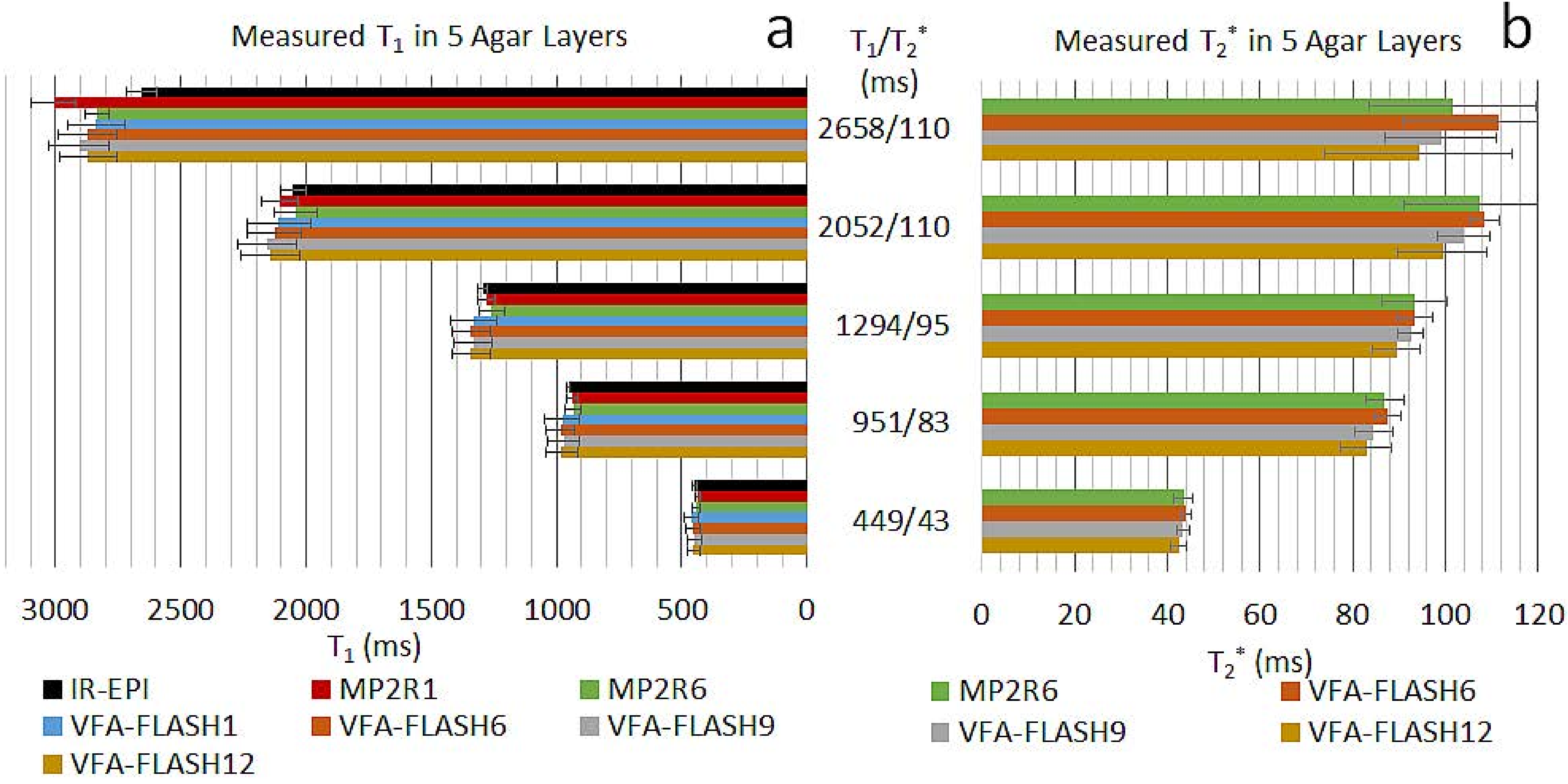
a
Measured T_1 in 5 Agar Layers
T_1/T_2^* (ms)
2658/110
2052/110
1294/95
951/83
449/43
3000
2500
2000
1500
1000
500
0
T_1 (ms)
IR-EPI
MP2R1
MP2R6
VFA-FLASH1
VFA-FLASH6
VFA-FLASH9
VFA-FLASH12
b
Measured T_2^* in 5 Agar Layers
0
20
40
60
80
100
120
T_2^* (ms)
MP2R6
VFA-FLASH6
VFA-FLASH9
VFA-FLASH12

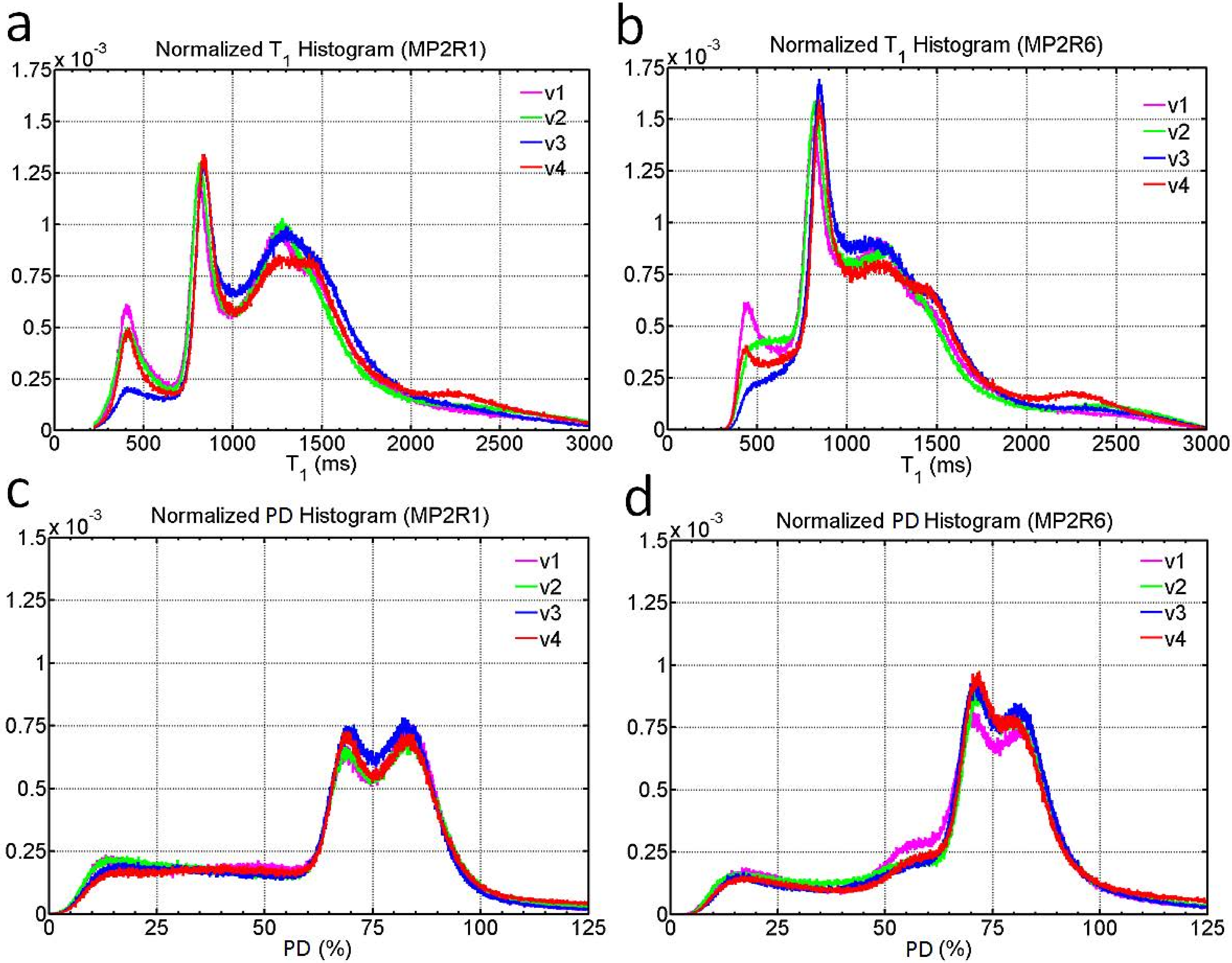
a
Normalized T_1 Histogram (MP2R1)
x 10^{-3}
T_1 (ms)
v1
v2
v3
v4
b
Normalized T_1 Histogram (MP2R6)
x 10^{-3}
T_1 (ms)
v1
v2
v3
v4
c
Normalized PD Histogram (MP2R1)
x 10^{-3}
PD (%)
v1
v2
v3
v4
d
Normalized PD Histogram (MP2R6)
x 10^{-3}
PD (%)
v1
v2
v3
v4

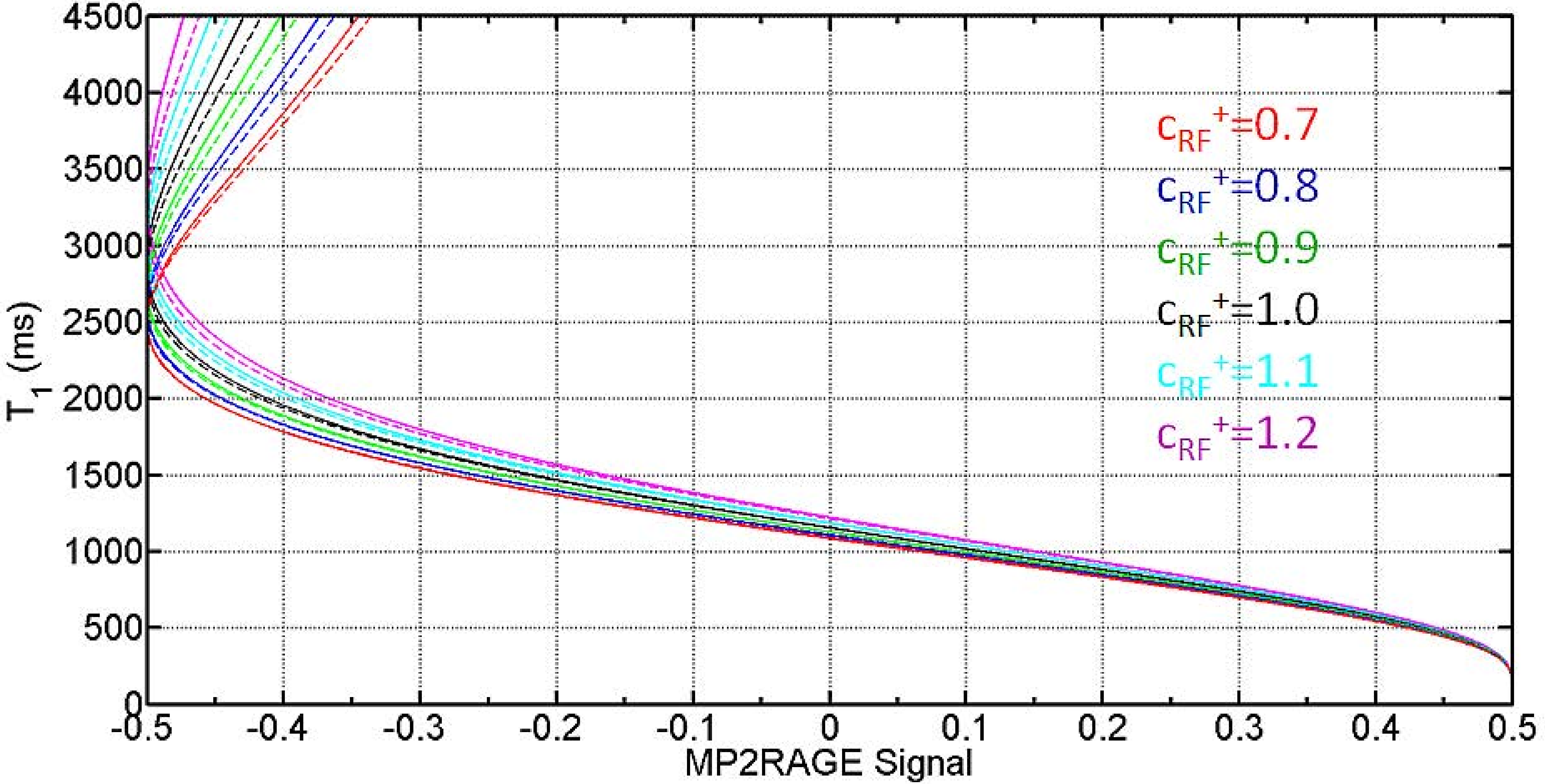

4500
4000
3500
3000
2500
2000
1500
1000
500
0
T1 (ms)
-0.5
-0.4
-0.3
-0.2
-0.1
0
0.1
0.2
0.3
0.4
0.5
MP2RAGE Signal
cRF+=0.7
cRF+=0.8
cRF+=0.9
cRF+=1.0
cRF+=1.1
cRF+=1.2